uOttawa

L'Université canadienne
Canada's university

University of Ottawa
Faculty of Engineering
Department of Civil Engineering

Validation of observed bedload transport pathways using morphodynamic modelling

Thesis of Master of Applied Science

Alexandre Mineault-Guitard

April 2016

Abstract

Braiding is a mesmerizing phenomenon since flow and sediment transport interact and are able to change the morphology of a channel in a rapid and complex fashion. Conventional two-dimensional morphodynamic models estimate bedload distribution using shear stress distribution. However, it is unclear if the use of such shear stress distributions is relevant or applicable for all situations when using two-dimensional morphodynamic modelling.

This thesis strives to investigate whether shear stress distributions are useful to predict bedload transport pathways. This study focuses upon prediction of bedload transport pathways using a morphodynamic model (Delft3D) of an anabranch of the Rees River (New Zealand). Observed bedload transport pathways were compared to modelled bedload transport pathways in an attempt to validate the predictive ability of the model. Results show that there is a significant correlation between predicted bedload transport pathways and the apparent bedload transport pathways derived from the field measurements. Furthermore, bedload transport predictions were in good agreement with observed data in areas where the model's predictions of high shear stress were comparable to field observations. However, substantial bedload transport predictions in low shear stress areas were not adequately captured by the model, suggesting that the observed pathways were not due to high shear stress, but rather to other sediment supply sources.

Table of content

List of Tables

List of Figures

List of symbols and abbreviations

Acoustic Doppler current profiler	aDcp
Apparent bedload velocity	v_a
Coefficient of determination	r^2
Comparison of two correlation factors	Z
Cubic meter per second	cms
Correlation between adjacent bins	C
Density	ρ
Digital elevation map	DEM
Dynamic viscosity	μ
Estimate of the root-mean-square turbulence intensity for real fluctuations	σ_S
Flow depth	Y
Hertz	Hz
Hour	h
Kilogram	kg
Kilometer	km
Kinematic viscosity	ν
Mean absolute error	MAE
Mean bed elevation	z
Megahertz	MHz
Meter	m
Millimeter	mm
Minute	min
One-dimensional	1D
Number of bins in the vertical	N
Root mean square error	RMSE
Roughness value	k_s
Sample size	n
Second	s
Shear stress	τ
Shear stress at the boundary	τ_0
Shear velocity	u_*
Terrestrial laser scanning	TLS
Three-dimensional	3D
Two-dimensional	2D
Typical correlation	ρ_0
Vector correlation coefficient	ρ_v^2
Velocity measurements error of the aDcp	σ_ϵ
Uncertainty of an estimate of mean streamwise velocity out of a single-ping velocity measurement in a single bin	σ_u
von Karman constant	κ
Uncertainty of depth water velocity	σ_U
Water velocity	u
16^{th} percentile, median, 84^{th} and 90^{th} percentile diameter of sediment mixture	D_{16}, D_{50}, D_{84}, D_{90}

1. Introduction

1.1. Research Objectives and Thesis Structure

This study focuses on the prediction of bedload transport pathways using a morphodynamic model of an anabranch of the braided Rees River. Ultimately, this study aims to investigate whether shear stress distributions can be a useful tool to predict bedload transport pathways. Observed bedload transport pathways of the anabranch of the Rees River will be compared to modelled bedload transport results in an attempt to validate the pathways predicted by the model. Furthermore, measured and modelled shear stress distributions will be compared to measured and modelled bedload transport pathway locations to assess if high bed shear stress zones correlate with areas of bedload transport.

The following section presents a literature review of the relevant topics that are covered in the thesis, in order to demonstrate the need to study the relationships between observed shear stress distributions and the prediction of bedload transport pathways for braided rivers. Furthermore, a paper ready for publication which describes the work that was done as part of this study is also presented. Descriptions of the study area of the project, the data collection that was undertaken, as well as the numerical model used for this study are presented. The results of the analysis that were conducted are also presented in the paper, and followed by a discussion that includes assessment of shear velocity distributions and how those can be correlated to bedload transport pathways. Furthermore, the implications of using numerical modelling to predict bedload pathways are provided.

1.2.Braided Rivers and Sediment Transport Modelling

There are several types of rivers across the world. They present different characteristics depending on where they are located and in what conditions they are found. Braiding is a phenomenon where a river is characterized by multiple channel patterns, wide active and mostly un-vegetated floodplains (Belletti et al., 2015). Braided rivers constitute one of the three most common channel types found on Earth (Chalov & Alexeevsky, 2015) and the study of their morphology and morphodynamics has attracted many researchers worldwide. The following chapter will introduce braided rivers as well as describe what conditions are required in order to generate them. Moreover, sediment and bedload transport modelling, an important part of braided river morphodynamics modelling, will be introduced.

1.2.1. Causes of braiding

Braided rivers are mostly observed in proglacial mountainous regions, although they can also be found in lower gradient coastal or continental plains. As described previously, these rivers are characterized by a wide active floodplain having water flowing in several channels within them. Braiding can be mesmerizing since flow and sediment transport interact and are able to change the morphology of a channel in a rapid and complex fashion. Generally, braiding occurs due to high sediment supply in a channel or a river (Church, 1992). Some other phenomena involved include local scour and fill, channel bars development and migration, as well as bifurcation mechanisms (Ashmore, 2013; Belletti & al., 2015). The phenomena listed above are generated due to high stream power as well as low bed and bank erosion resistance relative to stream energy. This causes severe bedload transport within braided channels (Ashmore, 2013). In addition to the high stream power, mountainous braided rivers are

subject to extreme flow variability, floods and flow pulses, which create high sediment supply causing morphological changes in the floodplain (Caruso et al., 2013). Variability in the flows increases bedload transport, but this is not a condition for braiding (Murray & Paola, 1994). Furthermore, bedload transport can be observed at all flow stages, even at low flow far below bankfull conditions (Williams et al. 2015). Channels within the braided floodplain vary in scale and even lower flows are able to generate bedload transport in some smaller channels (Bertoldi et al., 2010). Thus, lower flows are not to be neglected when studying braided rivers.

Another factor influencing braided rivers is the presence of vegetation within the floodplain. Indeed, absent or limited in-channel or riparian vegetation will favor braiding by allowing lateral migration and channel widening (Ashmore, 2013). Furthermore, in-channel vegetated islands distinguish the two main types of braided river reaches, namely island-braided and bar-braided. Each reach of a braided river is defined as a river section composed of several channels that are divided at the upper boundary of the reach and reconnect at the downstream end (Chalov & Alexeevsky, 2015). The presence of vegetated islands creates more stable braided reaches (island-braided), whereas reaches with little to no vegetation are more subject to rapid morphological changes (bar-braided) (Belletti & al. 2015). Belletti & al (2015) summarized the controlling factors for braided rivers, depending on the type of braided reach (see Table I).

Table I – Controlling factors, positive (+) or negative (-), of braided rivers (adapted from Bellutti & al., 2015)

		Braided river patterns		
Controlling factors		Large island-braided	Multiple island-braided	Bar-braided
Space	**Stream power**	-	+	++
	Role of vegetation	++	+	-
Time	**Flow regime link to climate change**	-	+	+
	Time since last flood discharge	-	+	++
	Change in sediment supply	-	+	++

1.2.2. Sediment and Bedload Modelling

The use of numerical modelling to study rivers has increased in popularity over the last decades. Phenomena related to braiding make numerical modelling, more specifically sediment and bedload modelling, of braided rivers quite challenging. Indeed, numerous challenges are faced when modelling braided rivers such as the scale impact (either spatial or temporal) of morphodynamics. Some technical difficulties are linked to the models' spatial resolution, as well as the size and the extensiveness of field surveys. Channel surveys are either done such that a small area is analyzed to obtain high resolution data or to get coarser data for a larger area (Li et al., 2008). Moreover, channel surveying provides data for one point in time which is good to use for boundary condition purposes. However, one must use time averaged data in between surveys, which might not reflect the unsteady conditions that

occurred during that time. This might limit the predictive abilities of a model. These surveying difficulties are particularly acute for bedload measurements; conventional physical sampling techniques provide sparse point measurements with high sampling error (e.g., Rennie et al. 2002). A new surveying technique consists of using acoustic Doppler current profiler (aDcp) technology to gather direct bedload measurements (Rennie, 2002; Rennie et al., 2002). This technique can be used to obtain high resolution data over a larger area (Rennie and Church, 2010). However, it can lead to biased bedload measurements due to suspended sediments (Rennie & Millar, 2004).

Other challenges faced in braided river modelling are the simulation of flow, which is strongly affected by three-dimensional (3D) effects; and the development of a model that can simulate the numerous phenomena occurring in braided rivers (Nicholas, 2013). Most models created to study braided rivers are one-dimensional (1D) or two-dimensional (2D). Three-dimensional (3D) morphodynamics modelling tends to be less popular due to the high associated computational costs combined with a lack of precise data (Lane et al., 1999). Recent computational capacity advances have made it easier to study braided rivers using 2D and 3D models. This has resulted in better estimation and understanding of braided rivers' morphology, since braiding phenomena are difficult to estimate using 1D models. Sediment transport models, like the ones used to simulate braided flows, are usually depth averaged models, because of their simplicity and quickness (computational time) related to full 3D models (Fang, 2003). In depth averaged modelling, the determining variables, such as velocity, are averaged in one direction. In 2D depth averaged models for instance, the variables are averaged over the vertical axis (Islam, 2009). Thus, bedload transport is calculated from averaged values in such models. As stated above, morphological changes occur at various spatial scales such as local bed elevation fluctuations and channel migration.

Early studies of braided rivers were made at a scale of single bars because of the limited computing capacities of the time. However, it is now possible to study morphodynamics at larger scale. Indeed, whole braided floodplains and even large reaches are being analyzed in numerical studies (Nicholas, 2003; Williams et al. 2013; Williams, 2014).

1.2.2.1. 2D Morphodynamic River Modelling

The following section will describe the processes involved in morphodynamic models. Furthermore, some studies analyzing two-dimensional morphodynamic river modelling will be presented to guide the reader on what has recently been done on this topic as well as presenting the novelty of the present work.

Morphodynamic models are composed of several components that are combined in order to predict changes in a river's topography. The flow field is first predicted using a hydraulic model, which solves momentum and continuity equations. Bedload material transport is then calculated. Bedload transport formulas are usually derived from empirical experimentations or observations of a channel reach's average conditions. They are also known for their inabilities to produce accurate bedload transport predictions (Gomez and Church, 1989). Typical bedload transport modelling is based on excess shear stress, i.e. the amount of shear stress beyond the threshold shear stress required to mobilize bed particles. The shear stress at which bed materials start to be mobilized is defined as the critical shear stress. The critical shear stress depends on the resistance of particles to mobilization, which is a function of sediment size, as well as particle exposure. Van Rijn's (1984a,b,c) bedload transport formula, which uses the excess shear stress theory, is often utilised to determine bed load transport rate. Then, the suspended material load is predicted by modelling the advection and diffusion equation (Cao and Carling, 2003). Finally, local change in bed elevation can be

calculated from the sediment flux, calculated from the suspended and bedload transport, using the sediment continuity theory, also known as the Exner Equation. Thus, at each timestep the bed's topography is updated and used in the following timestep to estimate flow and sediment transport.

Emphasis towards 2D numerical modelling started in the early 1990s (Papanicolaou et al., 2008). It is around that period that initial investigations of two-dimensional sediment transport and morphodynamic river modelling started (Spasojevic & Holly, 1990; Chang, 1994; Chang et al., 1996; Lee et al., 1997; Walstra., 1998). Some studies even date back to the 1980s (Walters & Onishi., 1982). Today, 2D numerical models are still popular and are being used to simulate rivers' morphodynamics. Since 2000, several studies were carried to examine the sediment transport and morphology of rivers across the world, always bringing new techniques to improve the capabilities of morphodynamics modelling.

Chen and Duan (2008) proposed a way to model bank erosion and integrated it to a 2D depth-averaged model to simulate long term lateral migration processes of a meandering reach of the West Jordan River (United States of America). The model's predictions were adequate and replicated field measurements with good agreement. However, the model presented some limitations such as the inadequacy of modelling multiple grain-size and multilayered bank surfaces.

Vasquez (2005) developed a 2D movable-bed model that successfully reproduced laboratory experiments (Vasquez et al., 2005; Vasquez and Leal, 2006; Vasquez et al., 2007). This model was used to simulate modelling bed changes in meandering rivers, proposing unstructured grid and triangular finite elements (Vasquez et al., 2008). First, fixed bed level is assumed by the hydrodynamic model to compute the flow conditions. Water velocity and depth information are then transmitted to the movable-bed model to update bed topography.

The movable-bed model uses the sediment continuity (Exner) equation to compute bed elevation changes caused by bedload material transport. The model was tested using data from the Waal River (Netherlands). Results showed very good agreement between measured and modeled bed profiles and demonstrated the model's capacity to capture bed change features, such as bar formation (Struiksma, 1985).

Li and Millar (2007) modified an existing mobile-bed model (Danish Hydraulic Institute, 1999) to 1) account for multiple-size fractions and particle hiding effects; and 2) update the river bed bathymetry and surface grain-size distributions at each computational step. The modified model was used to simulate the lower Fraser River (Canada), and yielded good agreement with observed water level, bed shear stress and bedload rate. In another study, a gravel reach of the Fraser River was modeled using Li and Millar' (2007) model. It produced good agreement with the total sediment budget monitored in the field as well as the aggradation and degradation zones which were identified based on the longitudinal sediment transport gradient. The transport gradient is found by integrating bedload transport across the channel. Positive downstream gradients indicate degradation zones, whereas negative downstream gradients indicate aggradation zones. However, they found that bedload transport could not be handled effectively using cross-sectional or channel properties averaged data. They also proposed that when bed shear stress is used to predict bedload transport rate, it is important to differentiate bed shear that causes bedload transport and bed shear related to bed resistance on the flow. They note that shear stress and water depth are linearly dependant, thus a slight increase in shear stress will cause a modest water depth change. Bedload rate increases non-linearly with bed shear stress in excess of the critical shear stress for particle entrainment. To overcome this limitation which results in

overprediction of bedload rate, Li et al. (2008) proposed to use different friction coefficients for flow and bedload computations.

Braided rivers have also been studied, namely the Lower Yellow River in China (Wang et al., 2008) and New Zealand's Rees River (Williams et al. 2013; Williams, 2014). Wang et al. (2008) combined a 2D depth-averaged flow and sediment transport process model with a submodel for the bank retreat process. They used this model to simulate channel deformation in a braided reach of the Lower Yellow River. They found that their model was sensitive to the critical shear stress parameters, especially for bank soil. As a pre-cursor of the present study, Williams (2014) modeled a 2.5 kilometer (km) long braided reach of the Rees River. The model was used for depth-averaged morphological simulations of four high-flow events using the Delft3D model (Deltares, 2014). Results show that the predicted volume of erosion is within the observed volume uncertainty bounds, but that deposition estimations are slightly overestimated. Moreover, distribution of morphological change histograms show good agreement with observed data. On the other hand, cross-sectional comparison at a number of locations revealed poor agreement between predicted results and observed data. Williams explained that these discrepancies are due to the limitation of the angle of repose bank erosion algorithm of the model. Bank erosion is influenced by bedload transport due to shear stress acting on the bed, but also on the banks themselves; both of which are not represented in Delft3D depth-averaged simulations. Furthermore, the bank erosion algorithm, which is based on the angle of repose of the bank sediment, has limited predictive capacities due to the fact that physical representation of scour at the lower bank toe is not accounted for (Williams, 2014).

As introduced above, conventional 2D morphodynamics models use shear stress distribution to estimate bedload distribution (Li & al., 2008; Williams, 2014). However, field

evidence (Rennie, 2012, Williams et al. 2015) suggests that sediment supply locations, such as eroding banks, can dictate bedload transport pathways. Thus, it is unclear if the use of bed shear stress distributions is relevant or applicable for all situations when using 2D morphodynamics modelling.

1.3. Research Novelty

As previously mentioned, this study aims to identify whether shear stress distributions are useful to predict bedload transport pathways in braided rivers. Furthermore, observed bedload pathways will be compared to predictions from a morphodynamic model to evaluate the model's performance. This is the first study to test the morphodynamic model's capability to predict individual bedload transport pathways. This has not previously been possible due to lack of appropriate field data required for such validation.

Validation of observed bedload transport pathways using morphodynamic modelling

A. Mineault-Guitard, C.D. Rennie
Department of Civil Engineering, University of Ottawa, Ottawa, Ontario, Canada
R.D. Williams
School of Geographical and Earth Sciences, University of Glasgow, Glasgow, United Kingdom

ABSTRACT: Phenomena related to braiding, including local scour and fill, channel bar development, migration and avulsion, make numerical morphodynamic modelling of braided rivers challenging. This paper investigates the performance of a Delft3D model, in a 2D depth-averaged formulation, to simulate the morphodynamics of an anabranch of the Rees River (New Zealand). Model performance is evaluated using data from field surveys collected on the falling limb of a major high flow event, and using several sediment transport formulas. Initial model results suggest that there is generally good agreement between observed and modeled bed levels. However, some discrepancies in the bed level estimations were noticed, leading to bed level, water depth and water velocity estimation errors.

1. Introduction

Braided rivers constitute one of the three most common channel types found on Earth (Chalov & Alexeevsky, 2015). These rivers are characterized by multiple channels, as well as wide active and mostly un-vegetated widths. Braiding can be mesmerizing since flow and sediment transport interact and are able to change the morphology of a chanel in a rapid and complex fashion. Generally, braiding occurs due to high sediment supply in a channel or a river (Church, 1992). Processes involved include local scour and fill, channel bars development and migration, as well as bifurcation mechanisms. The phenomena listed above are generated due to high stream power as well as low bed and bank erosion resistance relative to stream energy (Ashmore 2013, Belletti et al. 2015).

The physical mechanisms of braiding make numerical modelling, more specifically sediment and bedload modelling, of this river style quite challenging. Some of the challenges

faced when modelling braided rivers include the spatial and temporal scales of morphodynamics. A model's spatial resolution and comparable extent, temporal frequency and accuracy of observational data for calibration can lead to other difficulties. Conventional topographical channel surveys are done such that larger areas are analyzed to obtain coarse data, while high resolution data are gathered for small areas (Li et al., 2008). However, the use of acoustic Doppler current profiler (aDcp) technology to obtain apparent bedload transport rates measurements, while water depths and velocities are concurrently acquired, provides a new approach to map channel morphodynamics (Rennie et al. 2002, Rennie and Church 2010, Williams et al. 2015). This method enables the direct measurement of bedload transport, but could possibly lead to biased bedload measurements due to suspended sediments loads (Rennie 2002, Rennie & Millar, 2004).

Most sediment transport models used to simulate braided rivers are depth-averaged models because three-dimensional (3D) morphodynamics modelling tends to be computationally expensive and 3D calibration data are often unavailable (Lane et al., 1999). However, braided river flows are strongly affected by 3D effects and bedload transport tend not to be handled effectively using averaged cross-sectional or channel properties data. On the other hand, two-dimensional (2D) models can account for secondary circulation and appropriate transverse and longitudinal bed shear stress vectors, which can contribute to adequate representation of the 3D complexity of morphodynamics. Bedload rate increases non-linearly with bed shear stress in excess of the critical shear stress for particle entrainment (Li et al., 2008). In many braided rivers, bedload transport is, however, not limited to bankfull flow, and bedload transport is observed at relatively low flows, far below bankfull conditions (Williams et al., 2015). Conventional 2D morphodynamics models use bed shear stress distribution to estimate bedload distribution. However, field evidence

suggests that sediment supply locations, such as eroding banks, can dictate bedload transport pathways (Rennie 2012, Williams et al. 2015). Thus, it is unclear if the use of bed shear stress distributions is appropriate for 2D simulations of braided river morphodynamics. This paper assesses the capability of a 2D morphodynamic model to predict observed bedload transport pathways and associated channel morphodynamics in a braided river anabranch.

2. Methodology

2.1. Study area

The Rees catchment is located on the Southern Island of New Zealand, as shown in Figure 1, and covers an area of 420 km^2 east to the Southern Alps (Williams et al., 2015). The Rees River is subject to high morphological activities, as described by Cook et al. (2013). The flow of the Rees River is strongly affected by storms, due to the steep slopes of the catchment and thin soil cover, resulting in steep rising limbs of flood hydrographs (Williams et al., 2013). The flow was monitored every 15 minutes from September 2009 to March 2011 at the Invincible gauging station, located about 8 km upstream of the study area (Williams et al., 2015). At this location, the Rees is confined to a single and un-vegetated channel (Williams, 2014). During that period, the mean discharge was 20 cubic meters per second (cms), with a peak flow of 475 cms. This study focuses on the single braid bar unit, shown in Figure 1, which represents approximately a 300 m portion of the river's main anabranch at the time of the surveys. Williams et al. (2013) summarized the hydrology of the Rees River, as well as provided some information about its bed composition.

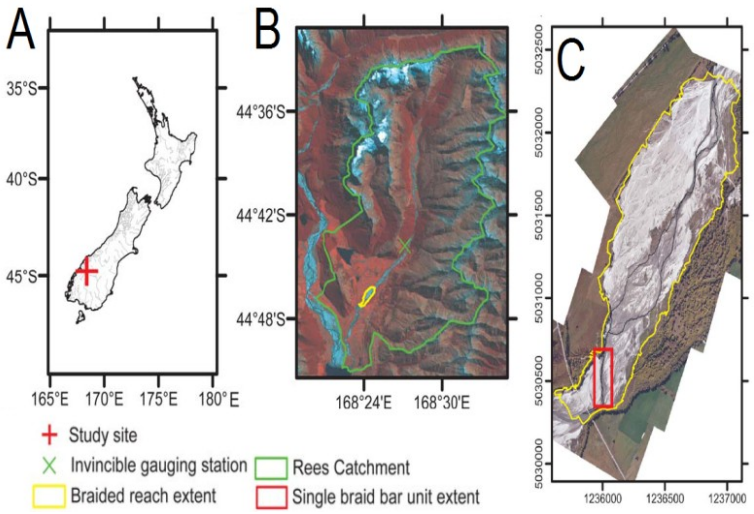

Figure 1 – A. Study area location. B. Rees catchment extent. C. Extent of study area (adapted from Williams et al., 2013)

2.2. Data Collection

The following section describes the processes that were followed to acquire field data for this study. The data collection processes were presented in Williams et al. (2013), Williams (2014), and Williams et al. (2015) but are summarized below. First, aDcp surveys were conducted to obtain hydraulic measurements. Second, terrestrial laser scanning (TLS) surveys were performed to generate digital elevation maps (DEMs) of the study area. Finally, bed material sampling was conducted to obtain surface and subsurface grain size distributions.

2.2.1. Hydraulic measurements

The acoustic surveys were acquired using a Sontek M9 RiverSurveyor (3.0 MHz transducer) mounted on a Sontek Oceanscience Riverboat trimaran. This apparatus was used to measure depths and velocities, as well to track from which bedload transport pathways were derived.

The trimaran was deployed using two ropes and operators, standing on opposite sides of the river, moved the platform from one bank to the other in zigzag transects, with a nominal 1 to 2 m streamwise spacing. The trimaran's position was obtained with a Novatel RTK-GPS, which was corrected in real time from a base station with approximately 0.02 m positional accuracy. Water depth, surface elevation and 0.1 m vertical bins of velocity, in both x and y directions, were gathered in 1 Hertz (Hz) ensembles from a 10 Hz sampling. Water velocities were recorded when water depth exceeded 0.4 m. Bottom-track velocities and RTK-GPS positions were recorded simultaneously at 1 Hz sampling frequency. Bottom track data were obtained when water depth exceeded 0.3 m, providing the information required to calculate apparent bedload velocity (v_a).

The surveys were carried out between February 7 and 16 2011, as described in Williams et al (2015), and are named Surveys B, C and D. The surveys were conducted following a 475 cms event, representing the largest flood recorded on the Rees River over a period of 18 months (September 2009-March 2011) as shown in Figure 2.

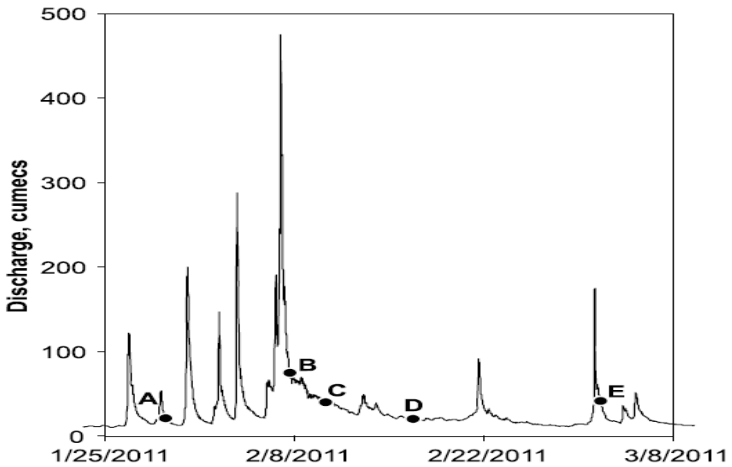

Figure 2 – Rees River hydrograph showing occurrence of surveys B, C and D (adapted from Williams et al., 2015)

Survey B was undertaken shortly after the peak flow, which resulted in noticeable discharge difference (4 cms) between the start and end of the survey. On the other hand, the flow remained somewhat constant during both Surveys C and D (Williams et al., 2015). Table 1 summarizes the relevant information from the surveys. The uncertainty shown for the discharges in Table 1 refer to one standard deviation of the mean measured discharge from at least four aDcp transects (Williams et al., 2013). Mean depth-averaged velocity for Survey C is higher that the measured depth-averaged velocity of Survey B, even if the measured discharge of Survey B is higher. This may be because the survey was restricted to the main anabranch. Furthermore, the average water depth during the surveys was approximately 0.47 m which makes this anabranch of the Rees River long (300 m) and shallow.

Table 1 – Characteristics of three water surveys of a Partial Braid Bar Unit of the Rees River (Williams et al., 2013)

Survey	B	C	D
Date and Time	07/02/2011, 16:00	10/02/2011, 7:35	16/02/2011, 17:10
Mean surveyed depth (m)	0.53	0.45	0.43
Mean surveyed depth-averaged velocity (m/s)	1.63	1.36	1.41
Discharge at upstream boundary of the survey (cms)	35.6 ± 0.9	23.6 ± 0.7	14.4 ± 0.7

2.2.2. Topography measurements

Topography of the study area was obtained from terrestrial laser scan (TLS) surveys using a Leica HDS6100 phase based TLS. Each scan was georeferenced using two targets that were positioned using RTK-GPS. For each topographic survey, between 14 and 20 scans were obtained from different locations with a maximum distance of 50 m between each location, leading to 10 to 15 million survey points. Two highly reflective targets were used to create a floating control network. The targets were set 10 to 15 m away from the scanner at a 120^{o} angle one to the other. The targets were positioned using a Leica 1200 GPS, which employs RTK processing, until a minimum point quality of 15 mm was achieved.

2.2.3. Bed material surveying

Surface material was obtained using the grid-count technique, equivalent to the pebble count technique proposed by Wolman (1954), leading to D_{16}, D_{50} and D_{84} estimations. Intermediate (b) axes of 100 clasts were sampled at evenly spaced increments within a 1 m^2 sampling frame. The sampling frame was positioned at 28 randomly selected sampling sites. Surface layer sampling was done in order to account for winnowing of fine surface material and resulting coarsening of the surface, as described in Klingeman et al. (1979) as well as Klingeman and Emmett (1982). Subsurface material sampling was done following Church et al.'s (1987) practical criterion of weighting 100 times the weight of the largest surface clast on the bar of interest. The depth of each sampling hole was estimated from the thickness of the most recently deposited sediment layer.

2.3. Delft3D Model

Delft3D, an open-source model managed by Deltares, was used to model morphodynamics of an anabranch of the Rees River. A 2D depth-averaged formulation was utilized, where Navier Stokes equations and Boussinesq approximation are solved by the model to simulate flow conditions under shallow water assumption. The model was run in unsteady mode with one depth-averaged layer. A 2D model was used since the Rees River, as mentioned earlier, is long and shallow. Thus, phenomenon occurring in the horizontal scale in the model is much more predominant over the vertical scale. More detailed model specifications are provided in Williams et al. (2013), as this model was used to replicate hydraulic conditions of the studied Rees River. The model was calibrated to three water surveys. Herein, the Delft3D model is applied to simulate morphological changes that occurred in-between the mentioned water surveys.

Delft3D computes sediment transport for suspended and bedload fractions. Suspended sediment transport accounts for cohesive suspended sediments ("mud") as well as non-cohesive suspended sediments ("sand"). Sand is also part of bedload sediment transport. However, the "bedload" sediment class computed by Delft3D refers to the sediments that are exclusive to bedload transport. Bedload transport, as analyzed by Delft3D, is obtained by looking at the magnitude and direction of bedload transport at each cell's centre. Then, the transport rates at the cell's interfaces are determined and corrected for bed-slope effect, upwind bed composition and sediment availability. At each computational timestep, bed elevation, at cell centres and interfaces, is dynamically updated. Thus, flow calculations done by the model are always based on adjusted bathymetry (Deltares, 2014). Bedload estimations depend on the prediction of shear stress. For the Van Rijn formula, bed shear stress is calculated using a quadratic friction law from the locally calculated depth-averaged velocity

and a drag coefficient that depends on the user-input bed roughness (k_s). Furthermore, the Van Rijn bedload calculation depends on the local calculation of bed shear stress from the hydrodynamic model, while accounting for difference between the user-input bed roughness and local grain roughness ($3D_{90}$) based on the bed material grain size distribution in the cell (Deltares, 2014).

Delft3D supports several sediment transport formulas. Some of these formulas, including the default Van Rijn (1993) formula, consider both suspended and bedload transport separately. Some formulas look at total sediment transport, suspended and bedload combined, while others analyze bedload transport only. A primary focus of this study was to investigate the impact of the type of sediment transport formula used by the model. Thus, the bedload transport formulas proposed by Wilcock-Crowe (2003) and Gaueman et al. (2009); the total transport formula proposed by Meyer-Peter and Müller (1948); and the bedload and suspended transport formula proposed by Van Rijn (1984a,b,c) were tested. The Wilcock-Crowe and Gaueman formulas were designed for transport of gravel-sand mixtures; the Meyer-Peter and Müller formula was based on experimental observations of gravel transport, while the Van Rijn's (1984a,b,c) was developed for sand transport.

2.4. General Model Setup and Inputs

The model was used to simulate morphological changes that occurred in-between the water surveys performed on the braided bar units of the Rees River. Data taken from three of the surveys were used as initial conditions and for comparison purposes. Thus, simulations were done to analyze two scenarios: Scenario 1 analyzed the morphodynamics that occurred between surveys B and C (3 days); while Scenario 2 looked at morphological changes

estimation between surveys C and D (6 days). Both scenarios were run using a timestep of 0.01 minutes (0.6 seconds) and a 480 minutes spin-up period before any morphodynamics calculation.

Unsteady discharge at the upstream boundary of the grid was estimated from the flow measured at the Invincible gauging station. Only three discharge values recorded at the upstream boundary of the study area (see Table 1) are available to correlate with the flow measured at the Invincible gauge. Flow estimations were achieved by both comparing the flow at Invincible at the time of the measurements (see Table 1) and by taking into account the time required for a water particle to travel from Invincible to the study area. First, Table 2 lists the flow recorded at the gauge station at the time of the surveys. The flow at the upstream boundary of the study area is 47%, 61% and 70% smaller than the flow at Invincible for Survey B to D, respectively. From these estimations, the flow at the upstream boundary of the model is, in average, 59% lower than at the gauging station. This is due to the fact that some flow is conveyed in minor anabranches outside of the study area.

Table 2 – Flow at Invincible at the time of the water surveys

Survey	Date and Time	Discharge at Invincible (cms)	Discharge at the upstream boundary (cms)	Difference (cms)	Difference (%)
B	07/02/2011, 16:00	75.00	35.60	39.40	47%
C	10/02/2011, 7:35	38.84	23.60	15.24	61%
D	16/02/2011, 17:10	20.70	14.40	6.298	70%

These estimates can be refined to account for unsteady discharge by considering the time required for a water particle to travel from the Invincible gauging station to the study area. Assuming that the gauging station is exactly at 8 km upstream of the study area, the traveling time of the water can be estimated using the mean surveyed depth-averaged velocity, as shown in Table 1. The time lags calculated are 1h22min, 1h39min and 1h35min for Survey B to D, respectively.

Table 3 shows the flow at the gauging station and the difference with the discharge recorded at the upstream boundary of the study area. The differences between the flows are, respectively, 47%, 62% and 70% for Survey B to D, thus an average difference of 60%. Thus, it would be adequate to assume that the flow at the upstream boundary of the study area is about 60% smaller than at Invincible. Therefore, flow measured at Invincible, recorded at a frequency of 15 minutes, lagged by 90 minutes and reduced by 60%, was set as the upstream discharge boundary. Furthermore, water level boundary conditions were set at the downstream boundary of the model.

Table 3 – Flow at Invincible considering time lag

Survey	Date and Time	Discharge at Invincible (cms)	Discharge at the upstream boundary (cms)	Difference (cms)	Difference (%)
B	07/02/2011, 14:38	76.18	35.60	40.58	47%
C	10/02/2011, 5:56	37.79	23.60	14.19	62%
D	16/02/2011, 15:35	20.64	14.40	6.24	70%

A flow versus water level relationship, also known as QH-relationship, was used at the downstream boundary of the model. Constant channel slope and roughness values, along with the assumption of a horizontal water surface, were used to calculate 1D discharge for different water levels. The mean slope of the profile, from upstream to downstream, is 0.004. The roughness value (k_s) used for the calculation a function of the bed material, was found by Williams et al. (2013) as part of an optimization analysis where the horizontal eddy viscosity, which is a measure of flow turbulence, was also calibrated. It was found that the optimal k_s value, which generated the optimal flow hydraulic predictions, was 0.04 m. Similarly, the optimal eddy viscosity was found to be 0.10 m^2/s(Williams et al., 2013). Confirmation of those optimal values for both k_s and eddy viscosity are presented in Section 3.1. The QH-relation was calculated from a cross-section of the river, near the downstream boundary. The cross-section was divided into segments, then the mean depth, area, conveyance and flow were calculated for all segments. From this, discharges were estimated for different water levels. Two flow versus water level relationships were developed, one for both Scenarios, and are presented in Table 4. A second option was considered as the forcing type of water levels at the model's downstream boundary. A timeseries option can also be used to set the water levels at the initial step and at the final step of the simulation, based on field measurements. Water levels during the simulation were linearly interpolated. Results showed that the two options yielded similar results. A flow versus water level boundary type is more representative of what would have been observed in the field, since the water levels set using the timeseries option are decreasing linearly from the start to the end of the simulation. Consequently, the QH-Relation option was used for the modeling, since it replicates with better precision the actual behaviour of the water level at the downstream boundary depending on the discharge in the river.

Table 4 – QH-relationships

	Scenario 1	Scenario 2
Water Level (m)	**Discharge (cms)**	**Discharge (cms)**
333.15	0.005	0.009
333.20	0.185	0.137
333.25	0.727	0.541
333.30	1.636	1.366
333.35	2.915	2.607
333.40	4.568	4.262
333.45	6.653	6.329
333.50	9.182	8.808
333.55	12.106	11.699
333.60	15.395	15.004
333.65	19.024	18.715
333.70	22.977	22.806
333.75	27.239	27.254
333.80	31.797	32.042
333.85	36.642	37.155
333.90	41.763	42.583
333.95	47.152	48.314
334.00	52.802	54.339

Other model characteristics such as its sensitivity to numerical grid resolution were also studied in William (2014). The optimal grid resolution was found to be 2 m, for a total of approximately 36 500 grid points. Additionally, the upstream boundary of the grid is located far enough from the study area so that the modeled build up section does not interfere with the predictions. Moreover, the model's sensitivity to riverbed composition, including active and bed layer thicknesses, initial bed material composition and sediment mixture, was done to optimize the model's parameterization. Moreover, Williams (2014) found that an active layer of 0.25 m and a base layer of 10 m were preferable for the Rees River model. The composition of this active layer was taken from the surface layer measured grain size distribution, while the base layer was established based on the subsurface layer distribution.

Both layer compositions were divided into 6 fractions, ranging from fine sand (D50 = 0.000125 m) to medium cobble (D50 = 0.090500 m). Table 5 summarizes the active and base layer composition, showing sediment sizes and fractions of the layer.

Table 5 – Active and base layer compositions

Sediment fraction name	Sediment size (m)	Fraction of active layer (%)	Fraction of base layer (%)
Fine sand	0.000125	8.2	3.8
Medium sand	0.000500	9.6	11.7
Very fine gravel	0.002000	13.7	18.7
Medium gravel	0.008000	26.1	29.3
Very coarse gravel	0.032000	38.2	34.0
Medium cobble	0.090500	4.2	2.5

Input bedload transport was also applied at the upstream boundary of the model. The input bedload was estimated from the only attempt to approximate total load on the Rees River. This attempt was done on the rising limb of a 90 cms flow that occurred in March 2010. The total load following this event was estimated to be 2.2 kg/s, based on aDcp bedload velocity measurements calibrated with physical bedload sampling (Brasington, et al., 2011). Delft3D uses volumetric rate (cms) as unit for bedload input, thus the estimated total load, or mass rate, must be converted. Consequently, the total load estimate was divided by the volumetric mass of the incoming sediment. Using the dry bed density of the sediment (1994 kg/m^3), the input bedload can be estimated as 0.0011 cms. However, this input load is based on the 2.2 kg/s load measured on the rising limb of a 90 cms flow, which was assumed to be due to a 50 cms flow. However, the flows during both Scenarios are less than 50 cms.

Indeed, the mean discharge at the upstream boundary of the model is estimated to be 20.35 cms for Scenario 1 and 18.71 cms for Scenario 2. These discharges lead to input bedload of 0.0003277 cms and 0.0003013 cms for Scenarios 1 and 2, respectively. Moreover, the input bedload was initially estimated to be composed of half medium sand and half very fine gravel. This was further investigated and the sensitivity of the results concerning the distribution of the input bedload will be presented in Section 3.6.

2.5. Performance Assessment

Measured field data including water velocity, depth and bed elevations, as described in Section 2.2, were compared to predictions by the Delft3D model. Predicted and measured data were compared by calculating the mean absolute error (MAE) as well as the root mean square error (RMSE) and the coefficient of determination (r^2). The error statistics mentioned are defined in Table 6, where $x_{modeled}$ represents predicted depth, velocity or bed elevation and $x_{measured}$ symbolizes measured depth, velocity or bed elevation.

Table 6 – Error Statistic Formulations

Error Statistic	Formula
Mean Absolute Error (MAE)	$MAE = \frac{\sum_i^n \lvert x_{modeled} - x_{measured} \rvert}{n}$
Root Mean Square Error (RMSE)	$RMSE = \sqrt{\frac{\sum_i^n (x_{modeled} - x_{measured})^2}{n}}$
Coefficient of Determination (r^2)	$r^2 = 1 - \frac{\sum_i^n (x_{measured} - \overline{x_{modeled}})^2}{\sum_i^n (x_{measured} - x_{modeled})^2}$
Vector Correlation Coefficient (ρ_v^2)	$\rho_v^2 = Tr[(\Sigma_{11})^{-1}\Sigma_{12}(\Sigma_{22})^{-1}\Sigma_{21}]$
Comparison of Two Correlation Coefficients (Z)	$Z = \frac{z_1 - z_2}{\sigma_{z1-z2}}\ \sigma_{z1-z2} = \sqrt{\frac{1}{n_1 - 3} + \frac{1}{n_2 - 3}}$

To complete the model's assessment, modeled bedload pathways, obtained at the end of the simulations, were compared to the pathways derived from field observations through a vector correlation analysis (Crosby et al., 1993; Rennie and Millar, 2004). A vector correlation coefficient, denoted ρ_v^2, is calculated to assess the predictive abilities of the model to predict bedload transport pathways. The equation to calculate the vector correlation coefficient is shown in Table 6, where Σ_{ij} is the 2 by 2 covariance matrix of vectors *i* and *j*. For two-dimensional vectors, the vector correlation coefficient ranges from 0 to 2. The vector correlation results will determine if the modeled bedload pathways are significant and will be used to guide further model refinements. The significance of the coefficient depends on the sample size. For large sample size ($n > 64$), the significant value of the vector correlation coefficient is calculate as $\rho_v^2 = 9.488/n$, representing the chi-square value of four degrees of freedom at 95% of confidence (Crosby et al., 1993). Furthermore, the vector correlation coefficients obtained for different simulations were compared using the formula shown in Table 6 and discussed in Zar (1996) to assess whether the two correlations are significantly different. For this case, the variables z_i represent the square root of half of the calculated vector correlation coefficient values, so that the maximum value of the coefficients is 1. If the two correlations are significantly different, the calculated Z value obtained should be greater than the two-tailed critical values, namely $Z_\alpha(2)$ which is equal to $t_{0,05(2),\infty} = 1.960$ at 95% of confidence.

3. Results

The following section will present the different sensitivity analyses that were carried to calibrate the Delft3D model. First, the hydraulic model calibration, done as part of Williams et al. (2013), was verified. Secondly, several sediment transport formulas were analyzed in order to identify the one generating the best predictions, as introduced in Section 2.3. Moreover, different boundary conditions were tested, both at the upstream and downstream end of the modeled area, and will also be presented. Finally, results of the sensitivity analysis on the parameters of the chosen sediment transport formula will be presented.

3.1. Validation of the Calibration of the Hydraulic Model

First, the hydraulic part of the Delft3D model was calibrated. This was done similarly as stated in Williams et al. (2013), in order to confirm the optimal values that were found for both bottom roughness coefficient and for eddy viscosity. This calibration process was done by comparing predicted water velocities and depths to their respective measured field data. The model was run using initial data from all three surveys. The simulations were run for a computational time of 24 hours, in order to ensure that steady state conditions were reached before the end of the simulations. Bottom roughness values from 0.02 to 0.14 m were analyzed, while eddy viscosity between 0.005 and 5 cms were studied. A constant eddy viscosity of 0.10 cms was used while analyzing the model's sensitivity to bottom roughness. On the other hand, a bottom roughness of 0.04 m was used as part of the sensitivity analysis of the eddy viscosity parameter. As shown in Table 6, the model's predictions were analyzed by calculating the MAE, the RMSE and the r^2. Table 7 and Table 8 list the statistical results

obtained from the bottom roughness calibration, for velocity and depth comparison respectively, allowing comparison of modeled predictions to actual field measurements.

Table 7 – Bottom Roughness Coefficient Calibration: Velocity Comparison

	Survey B			Survey C			Survey D		
k_s (m)	r^2	RMSE (m/s)	MAE (m/s)	r^2	RMSE (m/s)	MAE (m/s)	r^2	RMSE (m/s)	MAE (m/s)
0.02	0.5920	0.4320	0.3151	0.5864	0.3292	0.2551	0.5080	0.3166	0.2448
0.04	0.6353	0.3733	0.2772	0.6329	0.2475	0.1824	0.5112	0.2748	0.2057
0.06	0.6565	0.3538	**0.2735**	0.6563	0.2124	0.1514	0.5201	**0.2689**	**0.2025**
0.08	0.6663	**0.3499**	0.2798	0.6747	0.1969	**0.1397**	0.5254	0.2769	0.2127
0.10	0.6752	0.3516	0.2880	0.6825	**0.1955**	0.1415	0.5340	0.2874	0.2261
0.12	0.6809	0.3569	0.2970	0.6858	0.2011	0.1503	0.5386	0.3010	0.2424
0.14	**0.6847**	0.3642	0.3063	**0.6899**	0.2094	0.1614	**0.5406**	0.3158	0.2594

The bold values in Table 7 and Table 8 represent the best statistical values for each survey. Data presented in Table 7 suggest that high roughness values lean to better correlation (high r^2). However, k_s values of 0.06 m generated less error in the prediction, as shown by the smaller MAE values. Smaller roughness values result in better water depth estimations. Moreover, water depths obtained from small roughness values present very small error. Thus, a k_s value of 0.04 m, as found by Williams et al. (2013), is somewhat a middle ground between the results obtained for velocity and depth. Consequently, a bottom roughness value of 0.04 m can be classified as optimal for this model.

Table 8 – Bottom Roughness Coefficient Calibration: Depth Comparison

	Survey B			Survey C			Survey D		
k_s (m)	r^2	RMSE (m)	MAE (m)	r^2	RMSE (m)	MAE (m)	r^2	RMSE (m)	MAE (m)
0.02	0.9476	0.0555	0.0418	**0.8902**	**0.0562**	**0.0393**	**0.8573**	**0.0551**	**0.0424**
0.04	0.9524	**0.0432**	**0.0328**	0.8880	0.0619	0.0441	0.8565	0.0564	**0.0424**
0.06	**0.9529**	0.0442	0.0353	0.8845	0.0710	0.0538	0.8545	0.0635	0.0504
0.08	0.9524	0.0502	0.0410	0.8811	0.0803	0.0637	0.8519	0.0715	0.0593
0.10	0.9516	0.0578	0.0480	0.8775	0.0889	0.0728	0.8505	0.0785	0.0666
0.12	0.9505	0.0658	0.0558	0.8735	0.0969	0.0812	0.8486	0.0854	0.0735
0.14	0.9496	0.0737	0.0635	0.8708	0.1041	0.0888	0.8466	0.0918	0.0799

A similar process was followed to evaluate the model's sensitivity to eddy viscosity. Calibration results for both velocity and depth are presented in Table 9 and Table 10. Again, bolded values represent the best statistical values for each survey. The results presented in Table 9 suggest that the model is not too sensitive to eddy viscosity. However, higher eddy viscosity, in this case 0.100 m^2/s, generated better velocity predictions.

Table 9 – Eddy Viscosity Calibration: Velocity Results

	Survey B			Survey C			Survey D		
Eddy Viscosity (m^2/s)	r^2	RMSE (m/s)	MAE (m/s)	r^2	RMSE (m/s)	MAE (m/s)	r^2	RMSE (m/s)	MAE (m/s)
0.005	0.6416	0.3702	0.2706	**0.6345**	0.2707	0.2018	0.5027	0.2940	0.2207
0.010	**0.6420**	**0.3699**	**0.2707**	0.6341	0.2696	0.2007	0.5048	0.2921	0.2197
0.025	0.6389	0.3711	0.2718	0.6341	0.2651	0.1970	0.5041	0.2898	0.2171
0.050	0.6367	0.3726	0.2752	0.6351	0.2581	0.1913	0.5073	0.2837	0.2125
0.100	0.6353	0.3733	0.2772	0.6329	**0.2475**	**0.1824**	**0.5112**	**0.2748**	**0.2057**
1.00	--	--	--	--	--	--	0.4603	0.2864	0.2208
5.00	--	--	--	--	--	--	0.2570	0.5174	0.4677

Results of the eddy viscosity calibration for water depth predictions also show that the model is not too sensitive to eddy viscosity. However, an eddy viscosity of 0.01 m^2/s generally produces better results, yet no substantial difference can be noticed, contrary to

what is observed for velocity results. Thus, the optimal eddy viscosity for this Delft3D model of the Rees River is 0.100 m^2/s, in agreement with the findings of Williams et al. (2013).

Table 10 – Eddy Viscosity Calibration: Depth Results

	Survey B			Survey C			Survey D		
Eddy Viscosity (m^2/s)	r^2	RMSE (m)	MAE (m)	r^2	RMSE (m)	MAE (m)	r^2	RMSE (m)	MAE (m)
0.005	0.9534	0.0433	0.0325	**0.8924**	0.0586	0.0411	0.8582	0.0547	0.0410
0.010	**0.9534**	0.0433	0.0325	0.8921	0.0588	**0.0432**	**0.8582**	**0.0548**	**0.0410**
0.025	0.9530	0.0434	0.0326	0.8912	0.0593	0.0417	0.8573	0.0552	0.0414
0.050	0.9518	0.0438	0.0330	0.8904	**0.0601**	0.0425	0.8566	0.0557	0.0418
0.100	0.9524	**0.0432**	**0.0328**	0.8880	0.0619	0.0441	0.8565	0.0564	0.0424
1.00	--	--	--	--	--	--	0.8422	0.0768	0.0630
5.00	--	--	--	--	--	--	0.8007	0.1325	0.1168

3.2. Initial Model Calibration

The discharge at the upstream boundary of the reach was estimated from the flow measured at the Invincible gauging station, located 8 km upstream, as described in Section 2.4. The model was run using an unsteady discharge, as well as an input bedload, which is set at the upstream boundary. Initial results showed that the use of a single upstream boundary, extending across the anabranch width, was not adequate for the model. Indeed, Figure 3 shows the velocity field obtained at the end of the morphodynamic simulation using a single upstream boundary. As shown by Figure 3, the model does not predict the presence of the bar in the anabranch. Note that the results presented in this section were obtained using the Van Rijn sediment transport formula.

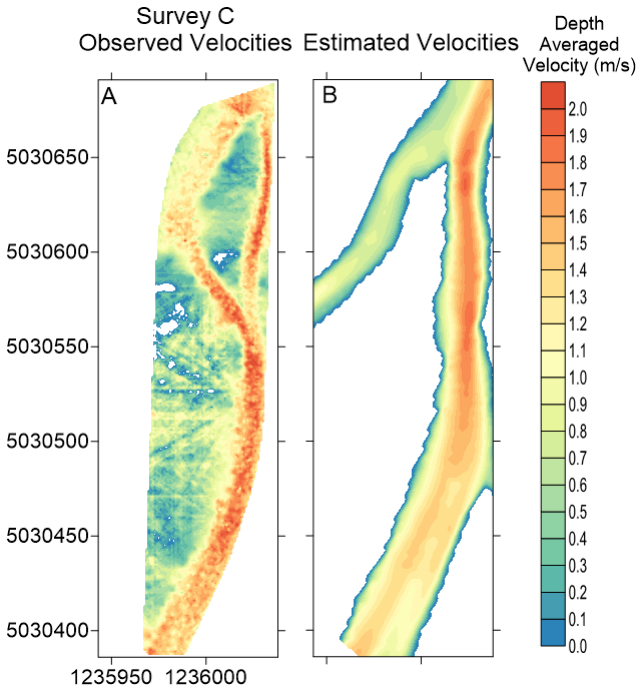

Figure 3 – (A) Observed Velocity Distribution Map for Survey C. (B) Velocity Distribution Maps Resulting from Morphodynamics Simulation Using a Single Upstream Boundary Across the Anabranch Width

It was observed that the morphological changes that occurred close to the upstream boundary of the model, further upstream of the results presented in Figure 3, were odd and caused by the input bedload, which is a fixed load across the boundary. Thus, it was decided to add a second boundary (upstream boundary B) at the upstream of the model. This addition was done in order to concentrate the incoming bedload in main section of the river (thalweg). Bedload is set as a volumetric rate across the width of the boundary. Upstream boundary B overlays the previously mentioned boundary (upstream boundary A) and the model uses its specifications to do the modelling in that part of the river. Figure 4 shows the numerical grid used by the model, as well as showing how the dual boundaries are defined. The discharge in

upstream boundary B was set as a discharge per cell, while a total discharge is set for upstream boundary A.

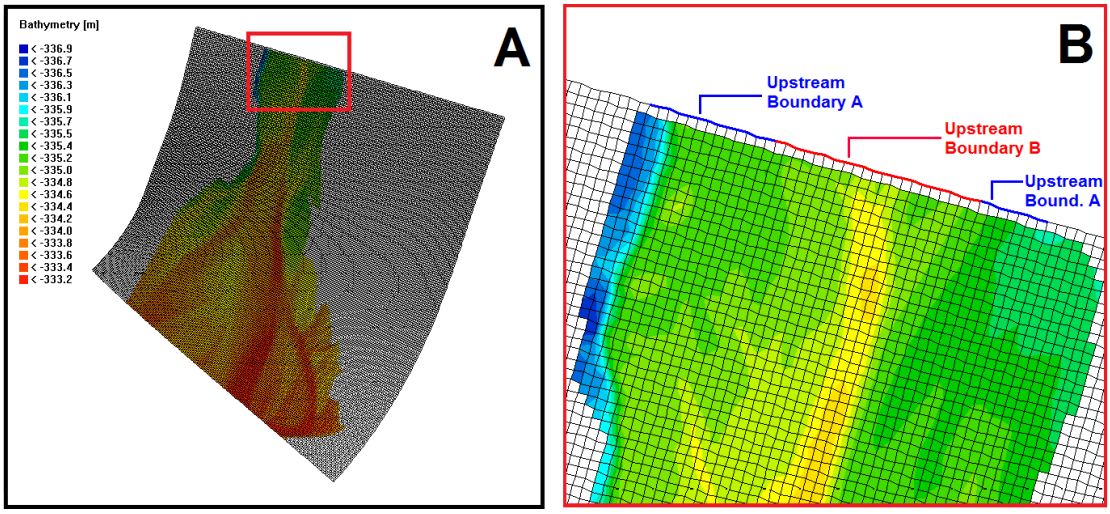

Figure 4 – (A) Numerical Grid and Bathymetry of Survey B (B) Upstream Boundaries Setup of the Model

The discharge per cell was obtained by estimating the percentage of flow in the main portion of the river at the upstream end of the study area. Once the percentage of flow was estimated, it was redistributed equally in the cells of upstream boundary B. Please note that the discharge per cell values remains unsteady. The model then calculates the remaining total discharge to set in upstream boundary A, in the portion not overlaid by upstream boundary B, from the forced total discharge. This setup makes the model more complex, but it leads to better morphodynamics in the region close to the upstream boundary of the model. Initially, it was estimated that the sum of the discharge per cell of upstream boundary B represents 60% of the flow at the upstream boundary of the study area. Using this new boundary, the model was run for Scenario 1, using the model setup described in Section 2.4.

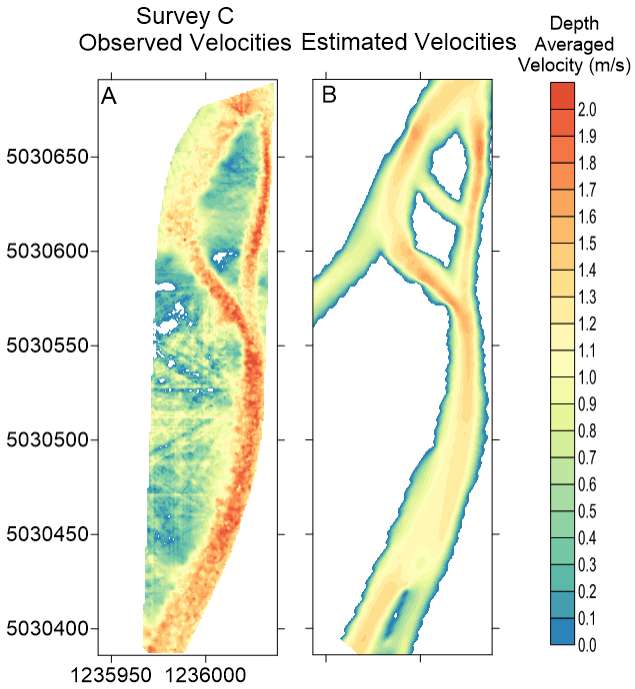

Figure 5 – (A) Observed Velocity Distribution Map for Survey C. (B) Velocity Distribution Maps Resulting from Morphodynamics Simulation Using Two Upstream Boundaries

Figure 5 presents the resulting velocity field at the end of the morphodynamics simulation using the new setup at the upstream boundary, as well as the observed velocity distribution map measured during Survey C. The addition of the new boundary changes the predicted flow field and the model now predicts the presence of the bar. Moreover, the resulting velocities are in good agreement with the observed data. However, the model predicts a channel allowing water to flow through the bar.

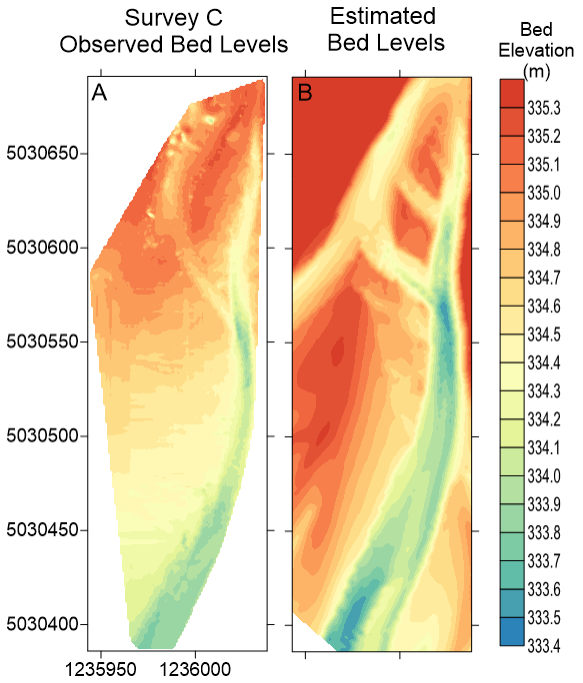

Figure 6 – (A) Observed Bed Level Distribution Map for Survey C. (B) Bed Level Distribution Maps Resulting from Morphodynamics Simulation Using Two Upstream Boundaries

Additionally, a low velocity zone is observed at the end of the study area, towards the left bank of the river. This is due to an overestimation of the bed elevations in that area, as shown in Figure 6. On the other hand, the resulting velocity field is still a good improvement from the one presented in Figure 3. The overestimation of the bed levels at the downstream end of the model is related to an overestimation of sediment deposition. To palliate this excessive deposition, a sediment bedload was forced at the downstream boundary. The imposed bedload at the downstream end of the model was estimated from the modelled bedload obtained as part of the results presented in Figure 3 and Figure 5. The forced bedload is composed of fine sand (0.00002 cms), medium sand (0.0005 cms) and very fine gravel (0.008 cms). Figure 7 shows the velocity distribution map generated using the results from

the simulation with the upstream boundary B, as well as the downstream forcing bedload transport condition.

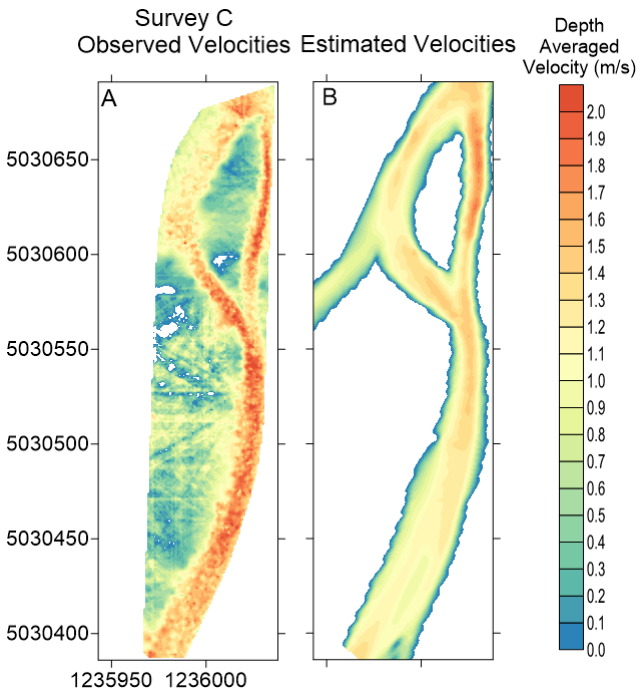

Figure 7 – (A) Observed Velocity Distribution Map for Survey C. (B) Velocity Distribution Maps Resulting from Morphodynamics Simulation Using Two Upstream Boundaries and Forcing Downstream Bedload

As presented in Figure 7, the addition of the downstream bedload condition reduces the deposition at the downstream end of the model, resulting in a smaller reduction in flow velocity in that portion of the river. Moreover, the imposition of the bedload at the downstream end of the model impacted the whole estimated bedload field. Importantly, the channel dissecting the bar is no longer present, providing a better match with the observed data.

3.3. Sediment Transport Formula Sensitivity Analysis

A major step of the calibration process was to identify the sediment transport formula which would most effectively model the morphodynamics that were observed between the field surveys. A total of four sediment transport formulas supported by Delft3D were analyzed, namely the Wilcock-Crowe (2003), Gaueman et al. (2009), Meyer-Peter and Müller (1948) and Van Rijn (1984a,b,c). The formulas were tested for Scenario 1 using the model setup described in Section 2.4. Note that here, the downstream boundary condition was forced using a fixed water level condition. Resulting water velocities and water depths at the end of the scenario were evaluated to the observed data. Moreover, the predicted bed levels at the end of the simulation were also compared to the surveyed elevations.

3.3.1. Numerical Analysis

The performances of all formulas are assessed numerically using the error statistics presented in Table 6. First, the estimated water velocity field resulting from sediment transport estimations, thus an estimation of the morphological changes that occurred during the scenario, is compared to the observed flow field of the Rees River measured during Survey C. Table 11 shows the statistics obtained from the different formulas for the water velocity component.

Table 11 – Numerical Performance of Sediment Transport Formula for Velocity Component

Formula	r^2	RMSE (m/s)	MAE (m/s)
Gaueman et al.	0.0833	0.4291	0.3442
Wilcock-Crowe	0.0456	0.4813	0.3565
Meyer-Peter and Müller	0.2883	0.4891	0.3812
Van Rijn	0.0936	0.6526	0.4926

Results shown in Table 11 suggest that the Meyer-Peter and Müller formula generates better correlation between the observed and modeled velocities. On the other hand, the Gaueman et al. formula resulted in smaller mean velocity errors, as both RMSE and MAE values are the smallest. Secondly, the same statistics were calculated from the comparison between observed and modeled water depths, as show in Table 12. Results presented in Table 12 show that all formulas give similar mean depth errors, but that the correlation of the modeled depths with observed depths is somewhat better using the Van Rijn formula.

Table 12 - Numerical Performance of Sediment Transport Formula for Depth Component

Formula	r^2	RMSE (m)	MAE (m)
Gaueman et al.	0.1439	0.2195	0.1875
Wilcock-Crowe	0.1504	0.2284	0.1905
Meyer-Peter and Müller	0.0647	0.2225	0.1647
Van Rijn	0.3512	0.2222	0.1809

Finally, the last comparison looks at the statistics of the predicted bed levels after the simulation. Table 13 shows the statistics obtained from the different formulas for the bed level component.

Table 13 – Numerical Performance of Sediment Transport Formula for Bed Level Component

Formula	r^2	RMSE (m)	MAE (m)
Gaueman et al.	0.8129	0.3069	0.2666
Wilcock-Crowe	0.8426	0.2665	0.2215
Meyer-Peter and Müller	0.8323	0.2239	0.1709
Van Rijn	0.7233	0.2615	0.2223

Results suggest that the Meyer-Peter and Müller formula leads to better estimation of the bed levels observed during Survey C. However, the other formulas give somewhat similar statistics as the values obtained using Meyer-Peter and Müller. Thus, analyzing the results using the numerical performances of each formula, the Meyer-Peter and Müller formula is the one which generates smaller mean errors for all variables that were analyzed.

3.3.2. Visual Interpretation

Observed and predicted distribution maps of all three variables analyzed in the last section will be presented in this section. This visual interpretation of the predicted results is done in order to confirm the results obtained in Section 3.3.1, since good statistics do not always translate into reasonable results. First, Figure 8 illustrates the velocities distribution map for

the observed data, as well as the resulting velocity distribution maps for the tested sediment transport formulas. Note that water is flowing from top to bottom on the figure.

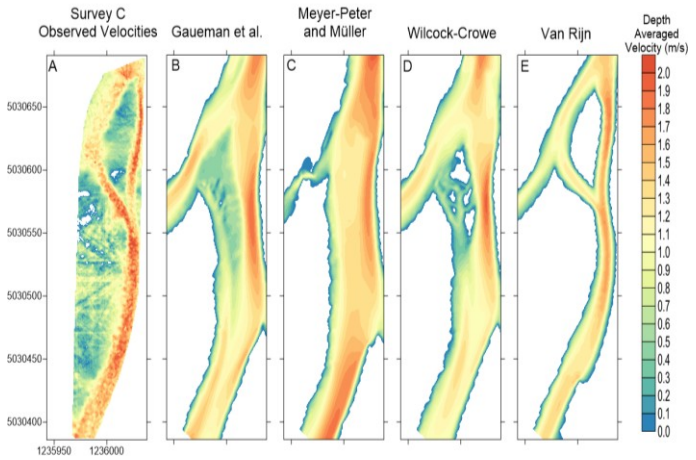

Figure 8 – (A) Observed Velocities Distribution Map for Survey C. (B-E) Velocities Distribution Maps Resulting from Morphodynamics Simulation for different Sediment Transport Formulas

One important note concerning the observed velocity distribution maps is related the side channel on the right bank of the river predicted by the model (B-E). The channel was present at the time of the measurements, but was not surveyed. Comparing the observed velocity field (A) to the other distribution maps, only the Van Rijn formula clearly indicates the presence of a bar near the upstream boundary and the flow that goes around this bar. Furthermore, the use of the Van Rijn formula results in better sediment transport estimations as the resulting velocity field, obtained from the predicted morphology, is better estimated than with the other formulas. Secondly, the same distributions maps were generated for the water depths, as shown in Figure 9. Similarly, the Van Rijn formula lead to better sediment transport estimations during the scenario, as the estimated water depths are in better

agreement with the observed data. The flow field is well replicated and the deep section of the river, downstream of the bar, is well captured by the model.

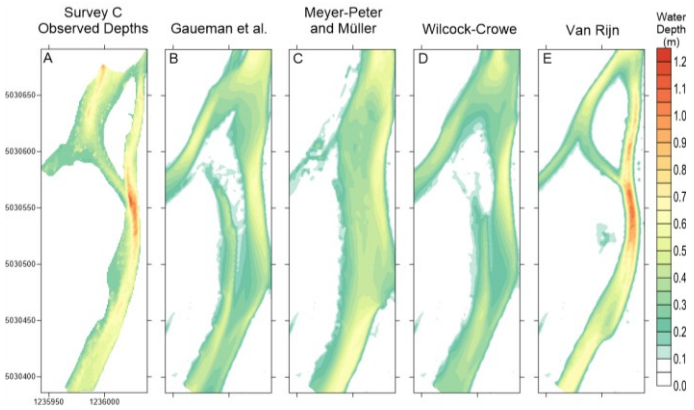

Figure 9 – (A) Observed Depths Distribution Map for Survey C. (B-E) Depths Distribution Maps Resulting from Morphodynamics Simulation for different Sediment Transport Formulas

The final bed elevations distribution maps, shown in Figure 10, were computed to visually compare the bed elevations measured during Survey C to the predicted bed levels at the end of the scenario. The distributed bed levels confirm that the use of the Van Rijn formula leads to better estimation of the morphodynamics that occurred in between Surveys B and C, since the predicted bed elevations are well replicated, compared to the estimations obtained with the other formulas. Thus, even if the Meyer-Peter and Müeller formula generated better estimation in a numerical point of view (see Section 3.3.1), the distributed maps of water velocity, depths and bed levels demonstrate that the Van Rijn's formula predictions seems better for the given Rees River reach.

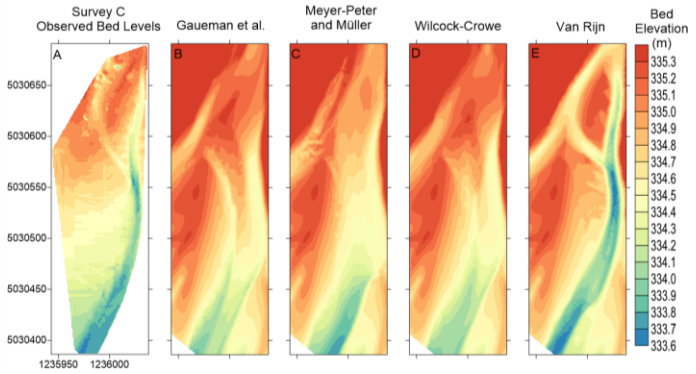

Figure 10 – (A) Observed Bed Levels Distribution Map for Survey C. (B-E) Bed Levels Distribution Maps Resulting from Morphodynamics Simulation for different Sediment Transport Formulas

In order to assess this given discrepancy between the numerical and visual results, the distributed difference maps between the observed and modeled results were computed. First, Figure 11 illustrates the difference between the observed and modeled velocity fields for all tested formulas. As shown in Figure 8, velocity resulting from the sediment transport predictions using the Van Rijn formula best replicated the general velocity field observed on site. Analyzing Figure 11, it appears that the low statistical values of the velocities obtained from the usage of the Van Rijn formula are due to the fact that the locations of the channels, following morphological changes estimated by the model, are slightly offset from the observed channel locations. Thus, the velocity values, following morphological changes using the Van Rijn formula, are close to the observed velocities, as shown by the white and light red zones delimited by the black lines (D). However, the location of the predicted channels differ from the observed ones, as shown by the blue zones (D), which lead to low statistical values listed in Table 11.

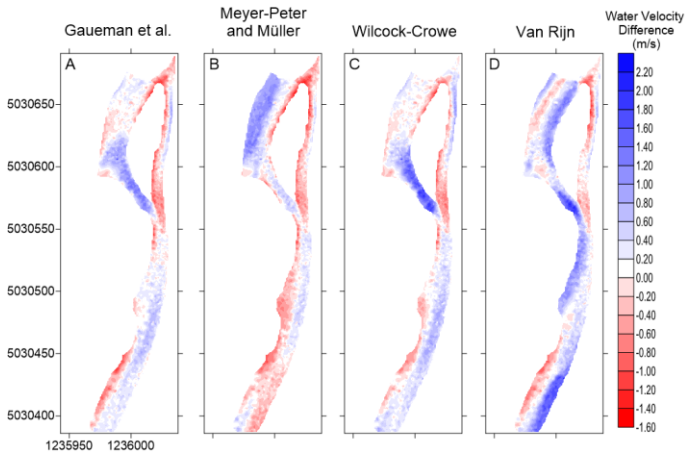

Figure 11 – (A-D) Difference Distribution Maps Between Observed and Resulting Velocities from Morphodynamics Simulation for different Sediment Transport Formulas

As for the Gaueman et al. and the Wilcock-Crowe formulas, they do not predict the confluence of the channels downstream of the bar, thus leading to high velocity differences in that zone. Although the Meyer-Peter and Müller formula yielded morphological changes that best estimate water velocities, it lead to underestimation of the flow in the channel on the right side of the bar and to overestimation of the flow over the bar. A similar process was done to analyze the areas where the depth and bed level predictions by the model differ from the observed data. Figure 12 shows the difference between observed and modeled water depths for the Rees anabranch. The distributed map illustrating the water depths difference obtained using the Van Rijn formula (Figure 12 D) shows that the predicted channels locations differ from the observed data.

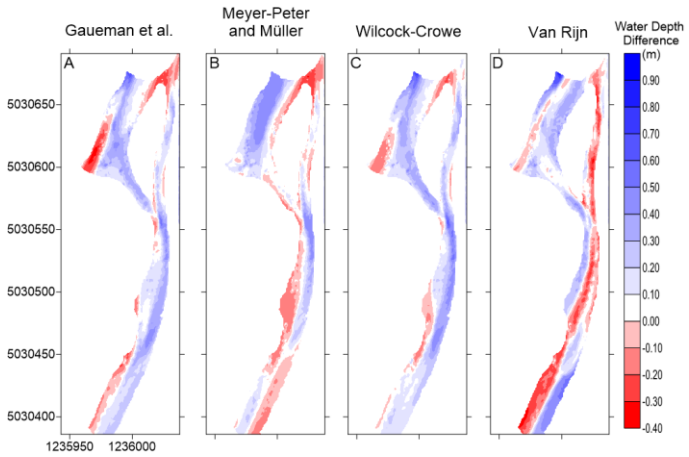

Figure 12 – (A-D) Difference Distribution Maps Between Observed and Resulting Depths from Morphodynamics Simulation for different Sediment Transport Formulas

Moreover, the water depths in the main thalweg of the river are overestimated using the Van Rijn formula. The morphological changes estimated by Gaueman et al. and the Wilcock-Crowe formulas lead to underestimation of the flow depth in the anabranch. As for the Meyer-Peter and Müller formula, it leads to underestimation the flow depths in the areas where the velocity estimations were close to the observed velocities downstream of the bar (Figure 11 B). Figure 13 shows the bed elevation differences between observed data and modeled results, as well as the difference between the DEM of Survey C and Survey B. All formulas, other than the Van Rijn, tend to overestimation of the bed elevations in the Rees anabranch. Indeed, the Van Rijn formula leads to underestimation of the riverbed throughout the anabranch, while the bed elevation predictions towards the left bank of the river at the downstream end of the reach are overestimated. However, comparing the modeled results (Figure 13 B-D) to the DEM of difference between Survey C and B (Figure 13 A), only the Van Rijn formula predictions concerning the erosion and sedimentation areas are comparable to what was observed.

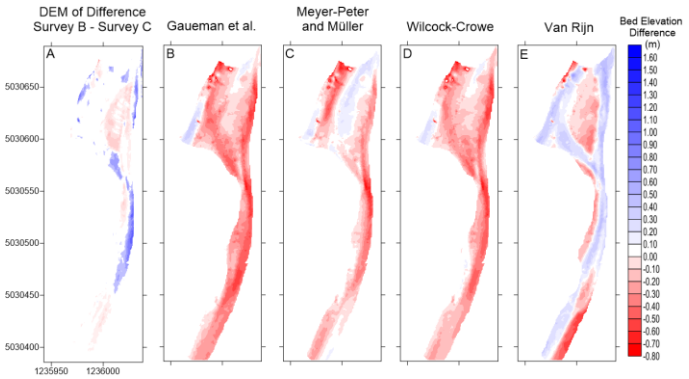

Figure 13 – (A) DEM of Difference between Survey C and B (B-E) Difference Distribution Maps Between Observed and Resulting Bed Elevations from Morphodynamics Simulation for different Sediment Transport Formulas

Similar to the observation that was made analyzing Figure 11, the low statistical values obtained using the Van Rijn formula, presented in Table 11 to Table 13, are linked to misprediction of the channel locations, since the resulted velocities, depths and bed levels do favor the Van Rijn formula when the results are visually compared to the observed data (Figure 8 to Figure 10).

3.4. Van Rijn Formula Parameter Sensitivity Analysis

As presented in the previous section, the Van Rijn sediment transport formula resulted in the best sediment transport predictions. Thus, it was used to run the Rees River Deflt3D model, as well as performing some other sensitivity analysis. However, the Van Rijn formula itself has some parameters that must be calibrated. Indeed, there are three parameters to be set while using the Van Rijn formula. First, a calibration coefficient, affecting suspended load transport, must be set. Secondly, a reference level (m) or roughness height value should be determined. Finally, a settling velocity (m/s) also needs to be set. The initial values for those

parameters, which were used for the Van Rijn results presented previously, are the following: calibration coefficient of 1.00; a reference height equals to 0.040 m; and a settling velocity value of 0.003 m/s. The reference level value was set to the bottom roughness found in Section 3.1, while the settling velocity of 0.003 m/s was calculated for a fine sand particle. Sensitivity analyses were done in order to identify if the initial assumptions for the Van Rijn's parameters are correct. The following sections will discuss the calibration done on the reference level and calibration coefficient parameters only.

3.4.1. Reference Level Sensitivity Analysis

The following section presents the sensitivity analysis that was done to analyze the impact of the Van Rijn's reference level on the model's results. Section 3.4.1.1 discusses the numerical comparison between observed data and modeled results using different reference level values, while Section 3.4.2.2 presents a visual comparison of the results to the field measurements.

3.4.1.1. Numerical Analysis

Reference level values were tested from 0.035 m to 0.045 m. Table 14 lists the statistical values obtained from the use of the different reference levels when comparing resulting velocities, following sediment transport simulation, to observed velocities. Analyzing the statistics presented in Table 14, the velocities resulting from the morphodynamics simulation using a reference level value equal to the bottom roughness (0.04 m) are closer to the observed velocities.

Table 14 – Numerical Performance of Van Rijn's Reference Level Parameter for Velocity Component

Reference Level (m)	r^2	RMSE (m/s)	MAE (m/s)
0.035	0.1239	0.5020	0.4025
0.040	0.2155	0.4281	0.3451
0.045	0.1356	0.4689	0.3629

All calculated statistics are better for a reference level of 0.040 m when comparing the velocities obtained at the end of the scenario to the ones that were measured in the field during Survey C. Similarly, the statistical errors calculated between the observed and resulting water depths from the Van Rijn's reference level sensitivity analysis are listed in Table 15.

Table 15 – Numerical Performance of Van Rijn's Reference Level Parameter for Depth Component

Reference Level (m)	r^2	RMSE (m)	MAE (m)
0.035	0.3204	0.1886	0.1544
0.040	0.4401	0.1566	0.1257
0.045	0.4110	0.1660	0.1299

Reference levels of 0.040 m and 0.045 m lead to similar water depth estimations at the end of the simulation, as the obtained statistics are similar to one another. However, a reference level of 0.040 m generated better agreement between resulting water depths and observed water depths. Lastly, statistical values from the comparison between observed and modeled bed elevations are shown in Table 16. Bed elevations predicted using reference levels of 0.040 m and 0.045 m give similar statistics. However, a reference level of 0.040 m,

which is equal to the bottom roughness value used by the model (see Section 3.1), lead to better estimation of sediment transport in the studied anabranch.

Table 16 – Numerical Performance of Van Rijn's Reference Level Parameter for Bed Level Component

Reference Level (m)	r^2	RMSE (m)	MAE (m)
0.035	0.7513	0.3235	0.2899
0.040	0.8306	0.2976	0.2632
0.045	0.8092	0.2948	0.2639

3.4.1.2. Visual Interpretation

Distributed maps of the variables discussed and compared in the previous sections were generated to evaluate the impact of the reference level on the model's results from another angle. First, the observed velocities distribution map is presented in Figure 14, as well as the velocities estimated from the velocities obtained from the morphodynamics simulation. They show that all reference levels give similar velocity fields, comparable to the velocities observed during Survey C. However, reference levels of 0.035 m and 0.045 m lead to an extended low velocity zone at the downstream end of the study area, which was not observed during field measurements.

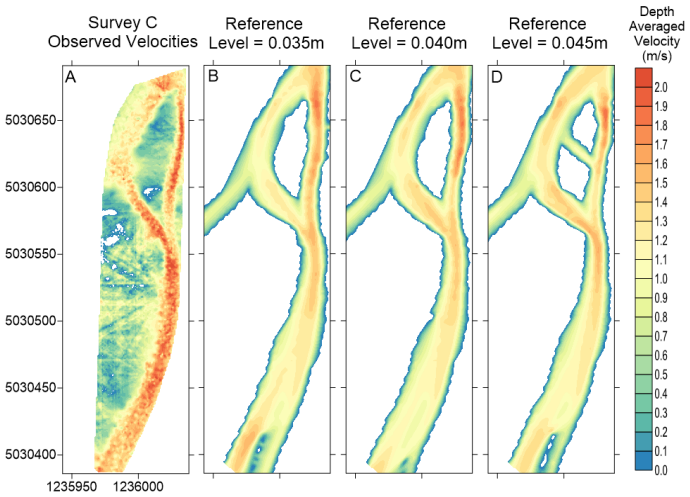

Figure 14 – (A) Observed Velocities Distribution Map for Survey C. (B-D) Resulting Velocities Distribution Maps of Morphodynamics Simulation for Van Rijn's Reference Level Analysis

Moreover, a reference level of 0.045 m lead to water flow through the bar, unlike what was observed. Finally, the resulting velocities using a reference level of 0.040 m generally replicated the observed velocities, although velocities were still somewhat underestimated. Similar maps were generated to compare water depths obtained using the tested reference levels to the observed depths, as shown in Figure 15. Analyzing the water depths maps shown in Figure 15 lead to similar observations. A reference level of 0.040 m lead to better agreement between observed and predicted water depths obtained at the end of the scenario, as it does not predict an extended low velocity zone near the downstream of the anabranch, contrary to the other reference levels.

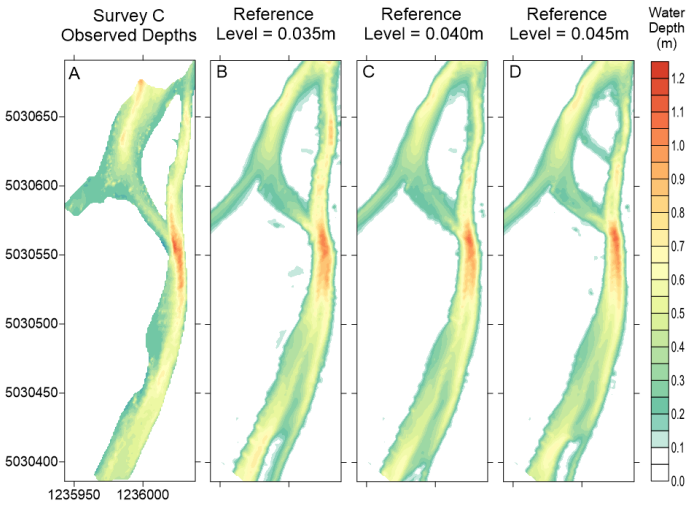

Figure 15 – (A) Observed Depths Distribution Map for Survey C. (B-D) Resulting Depths Distribution Maps of Morphodynamics Simulation for Van Rijn's Reference Level Analysis

Finally, Figure 16 compares modelled bed elevations using different reference levels to the bed levels measured during Survey C. Modelled bed elevations distributed maps shown in Figure 16 are all in good agreement with the measured bed levels. However, the channel incised through the bar is clearly observable looking at the bed elevations obtained using a reference level of 0.045 m (Figure 16 D). Moreover, all reference levels results in underestimation of the bed levels downstream of the bar, at the confluence of the channels, as well at the downstream end of the study area, towards the right bank. On the other hand, sediment transport predictions result in overestimation of the bed elevations near the left bank of the river at the end of the study area, causing the low velocity zone presented in Figure 14. However, the reference level of 0.040 m leads to lower discrepancy between modelled and observed bed elevations at the end of the study area, leading to better statistics as shown in Section 3.4.1.1.

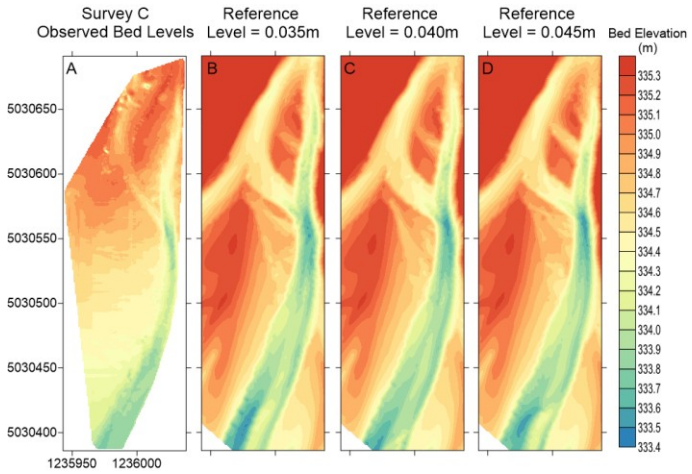

Figure 16 – (A) Observed Bed Levels Distribution Map for Survey C. (B-D) Resulting Bed Levels Distribution Maps of Morphodynamics Simulation for Van Rijn's Reference Level Analysis

3.4.2. Calibration Coefficient Sensitivity Analysis

Initially, the Van Rijn's calibration coefficient was set to be 1.00, thus not influencing the suspended sediment load or the model's results. However, a sensitivity analysis was done to assess the impact of the calibration coefficient on the model's results. Results are compared numerically (Section 3.4.2.1) and visually (Section 3.4.2.2) with observed data.

3.4.2.1. Numerical Analysis

The calibration coefficient was used to adjust the suspended transport load. This parameter was tested from values ranging from 0.85 to 1.05. Table 17 presents the statistical errors calculated from the comparison of the observed and the velocities obtained from morphodynamics simulations from different calibration coefficients tested. Calibration coefficients of 0.85 to 1.05 resulted in comparable velocities. On the other hand, the lowest

(0.80) and highest (1.05) values used for the Van Rijn's calibration coefficient lead to the poorest results.

Table 17 – Numerical Performance of Van Rijn's Calibration Coefficient Parameter for Velocity Component

Calibration Coefficient	r^2	RMSE (m/s)	MAE (m/s)
0.80	0.0939	0.5038	0.3931
0.85	0.1817	0.4573	0.3609
0.90	0.1652	0.4762	0.3742
0.95	0.1812	0.4564	0.3677
1.00	0.2155	0.4281	0.3451
1.05	0.1488	0.5150	0.4030

Furthermore, the initial calibration coefficient value of 1.00 resulted in somewhat better velocities, estimated from the predicted morphology at the end of the scenario, as all statistics are better than the ones obtained for the other calibration coefficients.

Table 18 – Numerical Performance of Van Rijn's Calibration Coefficient Parameter for Depth Component

Calibration Coefficient	r^2	RMSE (m)	MAE (m)
0.80	0.3716	0.1778	0.1420
0.85	0.3733	0.1732	0.1364
0.90	0.3714	0.1731	0.1372
0.95	0.3906	0.1713	0.1356
1.00	0.4401	0.1566	0.1257
1.05	0.3189	0.1918	0.1558

In a similar analysis, statistical errors calculated from the comparison of observed and resulting water depths from the use of different calibration coefficients are listed in Table 18.

Analyzing the statistical values presented in Table 18, water depths, estimated from the predicted morphology at the end of the morphodynamics simulations, are not too sensitive to the calibration coefficient values. However, the use of a calibration of 1.00 generated the best correlation between observed and resulting water depths, as well as smaller mean errors. Lastly, statistical values from the comparison between observed and predicted bed elevations are shown in Table 19.

Table 19 – Numerical Performance of Van Rijn's Calibration Coefficient Parameter for Bed Level Component

Calibration Coefficient	r^2	RMSE (m)	MAE (m)
0.80	0.7700	0.2770	0.2430
0.85	0.7928	0.2884	0.2579
0.90	0.7936	0.2837	0.2526
0.95	0.7873	0.2897	0.2586
1.00	0.8306	0.2976	0.2632
1.05	0.7668	0.3147	0.2782

Using the lowest calibration coefficient (0.80) lead to the best estimation of bed elevations, as suggested by the statistics listed in Table 19. On the other hand, a calibration coefficient of 1.00 lead again to the best correlation between observed and modelled results, while the discrepancies between observed and modelled bed elevations prediction were in average approximately 0.02 m more than when using a calibration coefficient of 0.80.

3.4.2.2. Visual Interpretation

To further analyse the impact of the calibration coefficient value on the model results, distributions maps of all three variables were generated. Thus, water velocities, depths and

bed elevations distributions maps are presented below. First, Figure 17 compares the observed velocity field to the velocity estimated from the resulting morphology at the end of Scenario 1. As shown in Figure 17, a channel, allowing water to flow through the bar, was predicted when using a calibration coefficient of 0.80, 0.85 and 0.95. Moreover, all tested calibration coefficients lead to velocity underestimation downstream of the bar. On the other hand, the velocity field at the downstream end of the model obtained from the use of the calibration coefficient of 1.00 was the one which best replicated the observed data, as the calibration coefficients of 0.80, 0.85, 0.90 and 1.05 leads to an extended low velocity zone. Finally, the calibration coefficient of 0.95 did not lead to a low velocity zone as extended as some others coefficient values, but still resulted in a zero velocity zone in the center of the river at the very downstream end of the model.

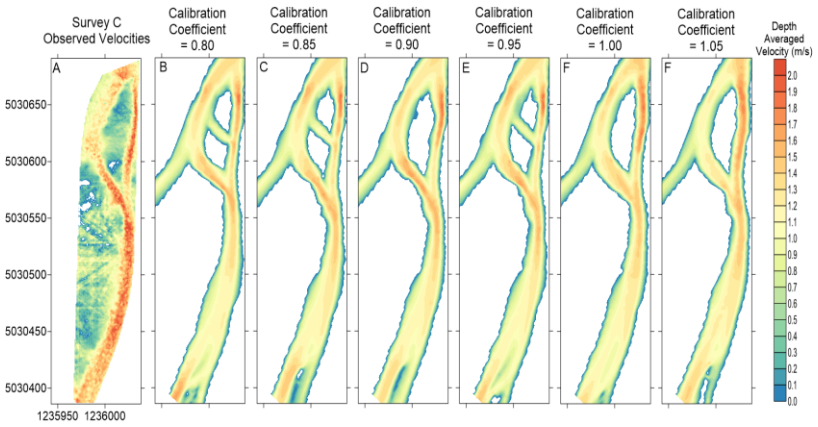

Figure 17 – (A) Observed Velocities Distribution Map for Survey C. (B-G) Resulting Velocities Distribution Maps of Morphodynamics Simulation for Van Rijn's Calibration Coefficient Analysis

Similar distributions maps were generated to compare water depths at the end of the simulations to the observed data. All tested coefficients values adequately predicted the

deepest water depths zone at the confluence of the channels, downstream of the bar. All calibration coefficients, with the exception of the calibration coefficient of 1.00, lead to a low water depth zones at the downstream end of the model, which was not observed during Survey C.

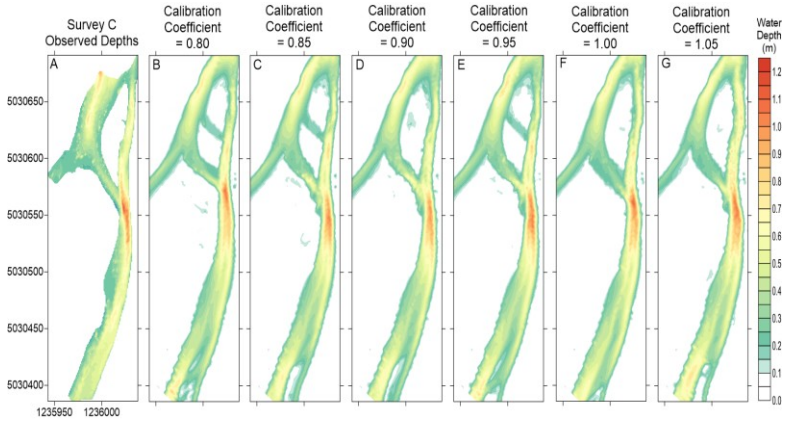

Figure 18 – (A) Observed Depths Distribution Map for Survey C. (B-G) Resulting Depths Distribution Maps of Morphodynamics Simulation for Van Rijn's Calibration Coefficient Analysis

Finally, observed and predicted bed levels obtained using different Van Rijn's calibration coefficients are compared in Figure 19. Bed elevations resulting from the use of a calibration coefficient of 0.80 best replicated the observed bed levels measured during Survey C, agreeing to the statistical values presented in Table 19. Morphodynamics simulation using a calibration coefficient of 0.80 did not result in underestimation of the bed levels downstream of the bar and at the downstream end of the model, contrary to the higher calibration coefficients tested. However, sediment transport resulting from the use the 0.80 calibration coefficient, as for the 0.85 and 0.95 coefficients, predicts a channel allowing water to flow through the bar, clearly observable in Figure 19 (B, C, E). Consequently, it was found that a

calibration coefficient of 1.00 was more suitable for the given Delft3D model of the Rees anabranch. The predicted morphology generated better velocity and water depths estimations, as well as leading to good agreement with observed bed elevations distribution.

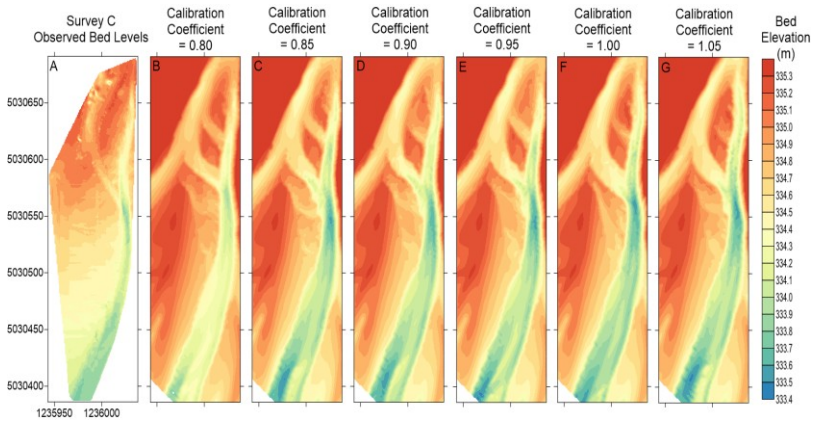

Figure 19 – (A) Observed Bed Levels Distribution Map for Survey C. (B-G) Resulting Bed Levels Distribution Maps of Morphodynamics Simulation for Van Rijn's Calibration Coefficient Analysis

3.5. Flow Fraction in Upstream Boundary B Sensitivity Analysis

The calibration of the upstream boundary B of the model (see Section 3.2) was another major step of the calibration process, since it is the location where discharge and bedload transport is set. Initially, it was assumed that 60% of the total flow going through the upstream boundary was flowing in upstream boundary B. The following section will discuss the discharge calibration at the upstream end of the model. Again, simulations were run for Scenario 1, using the model setup described in Section 2.4. For the following analysis, no bedload value was forced at the downstream end of the study area, contrary to the previous analyses, since the bedload magnitude depends on the discharge.

3.5.1. Numerical Analysis

In total, six different assumptions were made for the discharge fractions of the total discharge flowing through upstream boundary B: 50%, 55%, 60%, 65%, 70% and, finally, 75%. The model was run using the six different fractions in order to identify the one generating the best morphodynamics predictions, thus resulting water velocities, water depths and bed elevations estimations. First, Table 20 lists the statistical errors obtained when comparing the resulting velocities at the end of the morphodynamics simulations to the measured velocities.

Table 20 – Numerical Performance of Discharge Fraction at the Upstream Boundary for Velocity Component

Discharge Fraction	r^2	RMSE (m/s)	MAE (m/s)
50%	0.0818	0.6314	0.4726
55%	0.2551	0.4404	0.3513
60%	0.1136	0.5136	0.4034
65%	0.1490	0.4403	0.3425
70%	0.2036	0.4145	0.3418
75%	0.1834	0.4619	0.3817

As shown in Table 20, setting the flow fraction value in upstream boundary B at 50% of the total flow lead to higher mean errors. Moreover, the 55% and 70% flow fractions generated the best correlation between the observed and resulting velocities. However, having 70% of the total flow forced in upstream boundary B yielded better mean errors, as both the RMSE and MAE were the lowest of all tested flow fractions. On the other hand, discharge fractions of 55% and 65% lead to somewhat similar errors as the 70% flow fraction. Similar analysis was done in order to assess the model's performance for the depths estimated from the predicted morphologies using the several flow fractions mentioned

previously. As it was obtained for the velocity component, the highest correlation between observed and resulting water depths was reached using the 55% flow fraction at the upstream boundary B, as listed in Table 21. Moreover, the errors generated by the discharge fractions of 55%, 65% and 70% were similar, with a RMSE of approximately 0.16 m and a MAE of about 0.13 m.

Table 21 – Numerical Performance of Discharge Fraction at the Upstream Boundary for Depth Component

Discharge Fraction	r^2	RMSE (m)	MAE (m)
50%	0.2857	0.2194	0.1772
55%	0.4565	0.1622	0.1317
60%	0.3832	0.1781	0.1410
65%	0.3813	0.1656	0.1322
70%	0.3983	0.1600	0.1314
75%	0.3519	0.1915	0.1587

The bed elevation predictions were the final component compared with the observed data. The flow fraction of 55% set at the upstream boundary B again lead to the best correlation between the observed and predicted results. Contrary to the other components, bed elevations obtained from a flow fraction of 70% set for upstream boundary B did not generate the best predictions, as the RMSE and MAE values are better for the discharge fraction of 55%. Furthermore, mean errors obtained from the 60% to 70% flow fractions were similar to the errors for other flow fractions, while the 75% flow discharge again lead to somewhat lower statistics.

Table 22 – Numerical Performance of Discharge Fraction at the Upstream Boundary for Bed Level Component

Discharge Fraction	r^2	RMSE (m)	MAE (m)
50%	0.7887	0.2334	0.1942
55%	0.8160	0.2852	0.2477
60%	0.7617	0.3139	0.2797
65%	0.8059	0.3068	0.2739
70%	0.8127	0.3111	0.2717
75%	0.7287	03472	0.3098

3.5.2. Visual Interpretation

Distributed maps of the variables discussed and compared in the previous section were computed in order to evaluate the results visually. Thus, water velocities, water depths and bed levels distribution maps were plotted to visually compare the model's results to the observed data. First, Figure 20 shows the resulting velocities distribution maps for all tested discharge fractions at the upstream boundary B, as well as the observed velocity field of Survey C. Figure 20 confirms that having 50% of the flow set in upstream boundary B (Figure 20 B) lead to poor prediction of the velocity field, since the bar size was greatly underestimated. On the other hand, the 55%, 65% and 70% flow fractions velocities distribution maps were very comparable. However, sediment transport using 55% and 60% of the total flow going through the upstream boundary B predicted flow going through the bar, which was not observed during the survey. The flows near the downstream end of the anabranch were somewhat similar for all fractions as the flow was concentrated toward the right bank of the river. However, setting 50%, 60% or 65% of the flow for the upstream boundary B lead to a low velocity zone on the left bank at the very end of the study reach,

which was not observed during the field measurements (Figure 20 A), nor predicted by the model using the 55%, 70% and 75% flow fractions.

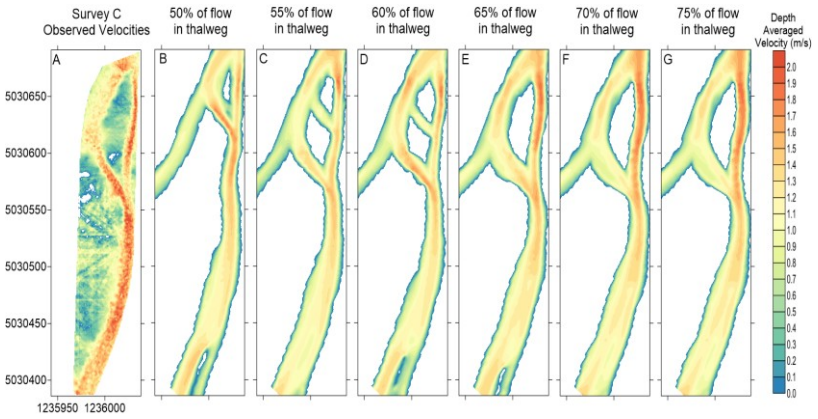

Figure 20 – (A) Observed Velocities Distribution Map for Survey C. (B-F) Resulting Velocities Distribution Maps of Morphodynamics Simulation for Discharge Fraction at the Upstream Boundary Analysis

As water velocities and depths are related, similar conclusions can be made by comparing resulting water depth fields with the observed data, as shown in Figure 21.

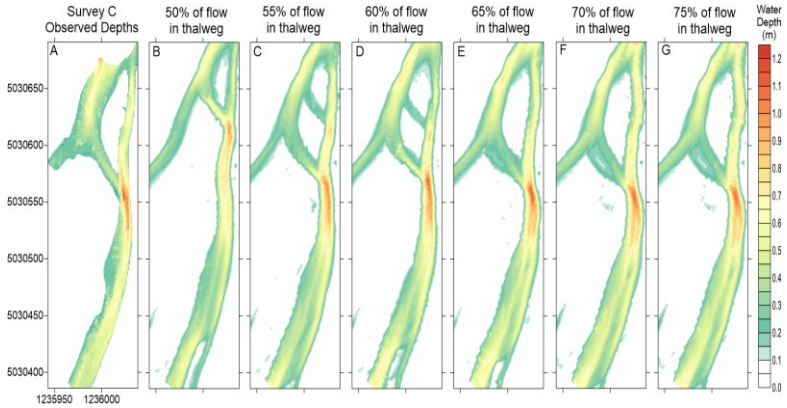

Figure 21 – (A) Observed Depths Distribution Map for Survey C. (B-F) Resulting Depths Distribution Maps of Morphodynamics Simulation for Discharge Fraction at the Upstream Boundary Analysis

Forcing 50% of the total flow in boundary B lead to large depth estimation errors, mostly due to the misprediction of the bar's position and size. Again, all tested flow fractions larger or equal to 55% were quite similar (Figure 21 C-F). Furthermore, discharge fractions of 55%, 70% and 75% were the only fractions which did not lead to an extended low water depth zone towards the left bank of the river at the downstream end of the study area. Finally, bed elevations at the end of the morphodynamics simulations were visually compared to the observed bed levels. Figure 22 (A) presents the observed bed levels for Survey C, as well as the resulting bed elevations (B-F), for all tested discharge fractions. The morphological changes resulting from forcing 50% of the total discharge in upstream boundary B were not well predicted by the model, as the size of the bar was greatly underestimated.

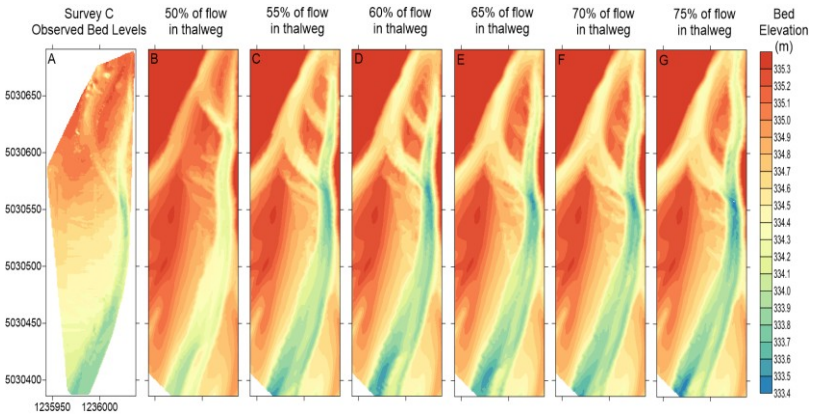

Figure 22 – (A) Observed Bed Levels Distribution Map for Survey C. (B-F) Resulting Bed Levels Distribution Maps of Morphodynamics Simulation for Discharge Fraction at the Upstream Boundary Analysis

Moreover, all flow fractions over 55% lead to overprediction of the erosion occurring in the thalweg, predicting lower bed elevations. On the other hand, sediment transport resulting from these flow fractions in upstream boundary B generated good estimation of the bar's size

and location. However, the 55% and 60% flow fractions lead to erosion within the bar, creating a small channel allowing water to flow through it. Furthermore, all flow fractions overestimated the bed elevations near the left bank of the river, at the downstream end of the study reach. However, flow fractions of 55%, 70% and 75% did not lead to low velocity and depth zones in that area of the anabranch, contrary to the other fractions. Thus, by analyzing the statistics shown in Section 3.5.1 and the figures shown in the present section, forcing 70% of the total flow at the upstream boundary of the model in upstream boundary B lead to better model predictions.

3.6. Model Input Bedload Calibration

The input bedload values were calculated and presented in Section 2.4 and are, respectively, 0.0003277 cms and 0.0003013 cms for Scenarios 1 and 2. However, the sediment distribution of these loads is unknown, thus several distributions were tested in order to identify the one leading to the best morphodynamics. It was assumed that the bedload transport was mostly composed of sediments ranging from fine sand to medium gravel, as introduced in Table 5. In total, 9 sediment distributions were analyzed and are presented in Table 23, where the percentage of each sediment fraction for all tested distributions is shown. For this sensitivity analysis, no bedload value was forced at the downstream boundary of the model. The percentages of the sediment fractions of Distribution 2 were the same, in proportion, to the ones of the bed composition (see Table 5).

Table 23 – Bedload Sediment Size Distributions

Distribution	Fine sand	Medium sand	Very fine gravel	Medium gravel
Distribution 1	0%	50%	50%	0%
Distribution 2	26%	30%	43%	0%
Distribution 3	0%	60%	40%	0%
Distribution 4	50%	50%	0%	0%
Distribution 5	0%	40%	60%	0%
Distribution 6	0%	0%	100%	0%
Distribution 7	0%	100%	0%	0%
Distribution 8	0%	0%	50%	50%
Distribution 9	0%	33.3%	33.3%	33.3%

3.6.1. Numerical Analysis

Similar to the previous analyses, the resulting velocity fields obtained using the tested distributions were compared numerically with the observed data, using the statistical errors listed in Table 6. Data presented in Table 24 shows that Distribution 2 is the distribution leading to the best correlation between observed velocities and the ones estimated from the predicted morphologies at the end of the scenario. On the other hand, the mean errors were the smallest using only medium sand (Distribution 7) as bedload. Distribution 6, which is composed of only medium sand, lead to mean errors comparable to the ones obtained using Distribution 7. Furthermore, the distribution with the largest amount of fine sand (Distribution 4) lead to the worst statistics.

Table 24 – Numerical Performance of Bedload Sediment Distribution Setup for Velocity Component

Distribution	r^2	RMSE (m/s)	MAE (m/s)
Distribution 1	0.1136	0.5186	0.4034
Distribution 2	0.2485	0.5352	0.4061
Distribution 3	0.1203	0.5006	0.3817
Distribution 4	0.1092	0.8573	0.7214
Distribution 5	0.0811	0.5162	0.3911
Distribution 6	0.1007	0.4921	0.3768
Distribution 7	0.1668	0.4627	0.3744
Distribution 8	0.0957	0.5157	0.3940
Distribution 9	0.1164	0.5175	0.3945

Next, the same analysis was done in order to assess the resulting model depths. The statistical values shown in Table 25 suggest that water depths obtained from Distribution 2 are more correlated with the observed water depths.

Table 25 – Numerical Performance of Bedload Sediment Distribution Setup for Depth Component

Distribution	r^2	RMSE (m)	MAE (m)
Distribution 1	0.3832	0.1781	0.1410
Distribution 2	0.4662	0.1924	0.1550
Distribution 3	0.3371	0.1795	0.1444
Distribution 4	0.2228	0.3055	0.2641
Distribution 5	0.3366	0.1799	0.1420
Distribution 6	0.3718	0.1758	0.1411
Distribution 7	0.3513	0.1763	0.1412
Distribution 8	0.2800	0.1948	0.1572
Distribution 9	0.3343	0.1841	0.1464

Furthermore, Distribution 6 and 7 lead again to the best estimation of the water depths, since their respective RMSE and MAE are the lowest of all distributions. Finally, bed elevation predictions were also compared to the observed bed levels, as shown in Table 26. Distribution 8, which was exclusively composed of gravel, half very fine gravel and half medium gravel, lead to the lowest estimation errors of the bed levels when compared to the measured data. However, Distribution 2 yielded similar RMSE and MAE values and has a better correlation. On the other hand, discrepancies of the bed elevation predictions using Distribution 7, the distribution which lead to the best velocity estimations, were on average approximately 0.07 m more than Distributions 2 and 8. Similarly, bed elevation errors using Distribution 6, are on average approximately 0.04 m more than the bed level predictions of Distributions 2 and 8. Distribution 6, as shown in Table 25, lead to the best water depth estimations.

Table 26 – Numerical Performance of Bedload Sediment Distribution Setup for Bed Level Component

Distribution	r^2	RMSE (m)	MAE (m)
Distribution 1	0.7617	0.3139	0.2797
Distribution 2	0.8064	0.2560	0.2152
Distribution 3	0.7878	0.3078	0.2753
Distribution 4	0.7274	0.2737	0.2186
Distribution 5	0.7684	0.3009	0.2663
Distribution 6	0.7925	0.2864	0.2547
Distribution 7	0.7802	0.3155	0.2838
Distribution 8	0.7838	0.2436	0.2120
Distribution 9	0.7781	0.2758	0.2425

3.6.2. Visual Interpretation

Distribution maps, for all three studied variables, were computed for the results presented in the previous section. Note that only the distribution maps for the Distributions 2, 6, 7 and 8 are presented below. Distributions 2 and 8 are the distributions generating the best bed elevation estimations while Distribution 6 and 7 give the best agreement between observed and resulting water velocities and depths. First, the velocity distribution maps are presented in Figure 23.

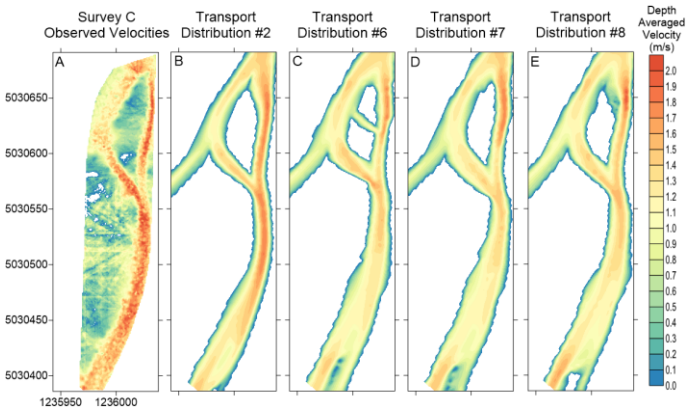

Figure 23 – (A) Observed Velocities Distribution Map for Survey C. (B-E) Resulting Velocities Distribution Maps of Morphodynamics Simulation for Bedload Sediment Distribution Setup Analysis

When comparing velocities estimated from the predicted morphologies at the end of the scenario to the observed velocity fields, there is a low velocity zone towards the left bank of the river for all presented distributions, which was not observed during the survey. However, this low velocity zone was more apparent using Distributions 6, 7 and 8. Moreover, velocities in the main thalweg were better estimated using Distribution 2. On the other hand, the bar width seemed to be slightly overestimated using Distribution 2. Sediment transport

predictions using Distribution 6 lead to a channel within the bar and flow connecting the two channels through the bar. Finally, the flow distributions of Distribution 7 and 8 were quite similar and were slightly underestimated in the thalweg region, but generally in good agreement with observed velocities. In a similar fashion, water depths distribution maps were computed (Figure 24) to visually compare the depths at the end of the simulations to the observed water depths of Survey C.

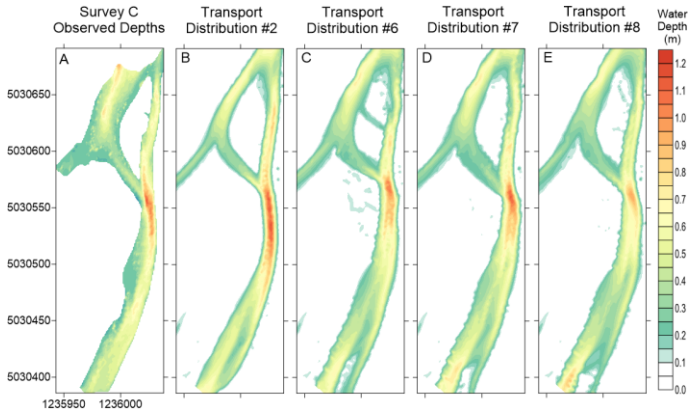

Figure 24 – (A) Observed Depths Distribution Map for Survey C. (B-E) Resulting Depths Distribution Maps of Morphodynamics Simulation for Bedload Sediment Distribution Setup Analysis

The resulting morphologies for all four distributions shown in Figure 24 adequately predicted the deep water depth zone downstream of the bar. However, Distribution 8 depths were somewhat underestimated in several zones, such as in the channel flowing on the right side of the bar, at the downstream of the bar and near the downstream boundary of the model. Moreover, the same low water depth zone at the downstream end of the anabranch was also observed in the distributed maps of Distributions 6 and 7. Sediment transport using Distribution 2 resulted in overestimation the bar's width, while being adequately predicted

for the other distributions. Furthermore, the predicted morphology using Distribution 2 slightly overestimated the water depths downstream of the confluence of the two channels. Lastly, modeled bed levels were plotted to compare visually the results with the observed bed elevations, as shown in Figure 25.

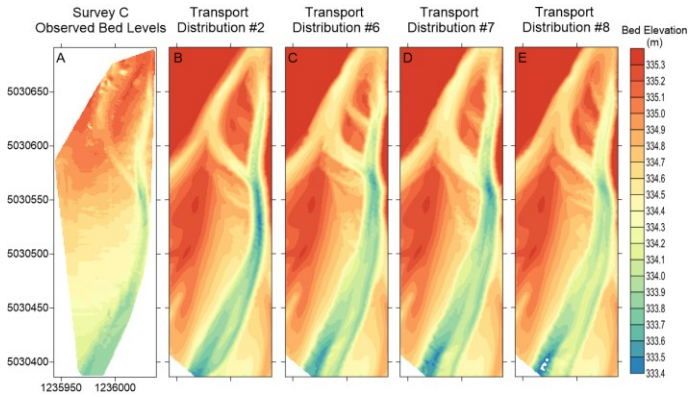

Figure 25 – (A) Observed Bed Levels Distribution Map for Survey C. (B-E) Resulting Bed Levels Distribution Maps of Morphodynamics Simulation for Bedload Sediment Distribution Setup Analysis

Sediment transport for all distributions seemed to predict adequately the lower bed elevations downstream of the bar. The use of Distribution 2 lead to bed levels that are somewhat lower than measured during Survey C in the main thalweg, downstream of the bar, while adequately estimating the bed levels in most of the anabranch. However, the estimated bar width were overestimated when using Distribution 2, thus leading to spatial offset of the channels, which might explain the higher MAE and RMSE values presented in Table 24 to Table 26. Sediment transport using Distribution 8 lead to overestimation of the erosion occurring towards the right bank of the river, at the downstream end of the study anabranch, thus to lower bed elevations in that area. This can also be observed in all other bed level

distribution maps, especially the ones representing Distributions 6 and 7 (Figure 25 C-D). Thus, from the statistical values presented in Section 3.6.1 and the figures presented above, Distribution 2 lead to best model predictions, especially near the downstream boundary of the anabranch, compared to the other distributions.

3.7. Identification of the Optimal Model Setup

The Delft3D model was subject to several sensitivity analyses, which were presented in the previous sections. The optimal setting for each analysis was identified; however, the optimal model setup must still be determined. The sensitivity analyses related to the Van Rijn's formula generated the best model predictions of all tested sediment transport formula. The sensitivity analyses related to the parameters of the Van Rijn's formula revealed that a reference level of 0.040 m and a calibration coefficient of 1.00 were the ones resulting in the best model predictions. The optimal Van Rijn's formulas were used as part of the other sensitivity analyses. Three cases were identified as the potential optimal setup for the Delft3D model. First, it was found that, while using sediment Distribution 1 as input load, forcing 70% of the total flow at the upstream end of the study area in upstream boundary B lead to the best model predictions out of all flow fractions tested (Case 1). Secondly, while forcing 60% of the flow through Boundary B, bedload input Distribution 2, the one in which the sediment fractions are in the same proportion as the ones of the bed composition, generated the best model predictions (Case 2). Lastly, a run combining the first two cases was tested. Thus, Case 3 uses Distribution 2 as the distribution for the input bedload of the model, while 70% of the total flow being forced in upstream boundary B. Similar to the previous analyses, this section compares the three cases numerically, then visually.

3.7.1. Numerical Analysis

The statistical values for the three cases described above were calculated to compare the model's results for one another. First, the statistics of the velocities, estimated from the predicted morphology of the anabranch at the end of the simulation, for the three cases are compared in Table 27.

Table 27 – Numerical Performance of the Three Optimal Model Setup for Velocity Component

Case	r^2	RMSE (m/s)	MAE (m/s)
Case 1	0.2036	0.4145	0.3418
Case 2	0.2485	0.5352	0.4061
Case 3	0.1162	0.6583	0.5192

As show in Table 27, combining the setting of the first two cases did not lead to better sediment transport estimations, as large estimation errors were generated, as seen for the resulting velocities of Case 3. The morphological simulation using Distribution 2 as the input bedload lead to better correlation between resulting and observed velocities. On the other hand, the smallest velocity errors between the observed data and the model results are obtained by Case 1. A similar comparison is presented in Table 28, where the water depths, based out of the morphology of the study area at the end of the simulation, are compared to the observed data. The water depths resulting from the predicted morphology of Case 3 have lower correlation with the observed data, as well as the highest mean errors.

Table 28 – Numerical Performance of the Three Optimal Model Setup for Depth Component

Case	r^2	RMSE (m)	MAE (m)
Case 1	0.3983	0.1600	0.1314
Case 2	0.4662	0.1924	0.1550
Case 3	0.3293	0.2358	0.1948

Depths obtained using the model's setup in Case 1 are the closest to the observed water depths during Survey C. However, Case 2 yielded depths that were most correlated with the observed data. Next, bed elevation predictions were compared numerically with the surveyed bed levels, as presented in Table 29.

Table 29 – Numerical Performance of the Three Optimal Model Setup for Bed Level Component

Case	r^2	RMSE (m)	MAE (m)
Case 1	0.8127	0.3111	0.2717
Case 2	0.8064	0.2560	0.2152
Case 3	0.6838	0.2930	0.2456

On one hand, the predicted morphology of Case 1, which lead to better velocity and depth estimations, was the one leading to the best correlation with the observed bed elevations. On the other hand, Case 1 also lead to the largest estimations errors out of the three cases. Case 2 generated bed elevations which were the closest to the observed bed levels, with a mean error of 0.2512 m, approximately 0.030 m less than for Case 3 and 0.057 m less than for Case 1. Finally, the resulting bedload transports pathways were compared to apparent bedload transport pathways obtained from Survey C. For this analysis, the 69 vector pairs

were compared, leading to an empirical significance threshold of 0.1375 in order to reach a 95% level of confidence. As shown in Table 30, all cases lead to bedload estimation that are significantly correlated with the apparent bedload transport pathways, since the resulting p_v^2 values were greater than 0.1375. However, Case 1 lead to the best correlation with observed data.

Table 30 – Comparison of Observed Apparent Bedload Transport Pathways to Predicted Bedload Transport Pathways for Three Optimal Model Setups

Case	Vector Correlation Coefficient Value
Case 1	0.3274
Case 2	0.2104
Case 3	0.2419

To determine if the predicted bedload pathways using Case 1 were substantially better than the predictions resulting from the other cases, the correlation coefficient values presented in Table 30

Table 30were compared, as presented in Table 6. Cases 2 and 3 were compared to the vector correlation coefficient value obtained for Case 1. The resulting Z values are listed in Table 31.

Table 31 – Comparison between Vector Correlation Coefficients

Comparison	Z Value
Case 1 VS Case 2	0.5349
Case 1 VS Case 3	0.3830

As shown, the bedload transports pathways predicted using Case 1 are not significantly different from the other cases, as the computed Z values are both smaller than the threshold

of significance (1.960). Thus, the predicted bedload pathways using Case 1 were not significantly better than the ones obtained from the other cases, but are still better correlated with the apparent bedload pathways derived from the field data measured during Survey C.

3.7.2. Visual Interpretation

In order to have a complete comparison between the three cases, the distributed maps of resulting water velocities, depths and bed elevations were generated and compared to the observed data. First, water velocities estimated from the predicted morphologies of all three cases were compared to the observed velocity field in Figure 26. The predicted morphology of Case 3 resulted in a narrow no flow zone near the end of the study area, which was neither observed during Survey C nor predicted by the other cases. Furthermore, the predicted bar using Case 3 seemed to be wider than the one observed during Survey C. On the other hand, the bar size and position were adequately predicted using both Case 1 and 2. Moreover, velocities resulting from Case 1 were underestimated downstream near the confluence of the two channels and downstream of the bar. Similar underestimation were observed when looking at the velocity field resulting from Case 2 (Figure 26 C), however the resulting velocities were somewhat closer to the those observed on the day of the survey. Lastly, the predicted morphology at the downstream end of the model for Case 2 lead to a small low velocity zone towards the left bank, which was not predicted using Case 1.

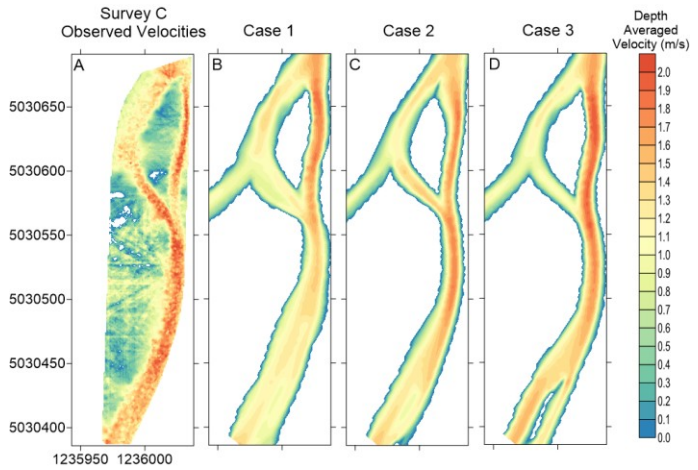

Figure 26 – (A) Observed Velocities Distribution Map for Survey C. (B-D) Resulting Velocities Distribution Maps of Morphodynamics Simulation Three Optimal Model Setup Analysis

Similar maps were generated to compare water depths resulting from all three tested cases to the observed depths, as shown in Figure 27. As previously mentioned, the predicted morphology using Case 3 generated a no flow zone near the downstream end of the study area. Moreover, Case 3's resulting morphology lead to overestimation of the water depths downstream of the confluence of the channels, as does the predicted morphology of Case 2. Sediment transport predictions from Case 1 adequately predicted the location and extent of the deepest section of the anabranch. Furthermore, the bar's size resulting from Case 1 seemed to be the closest to the observed bar, as Cases 2 and 3 overestimated its width. The predicted morphologies of Cases 1 and 2 lead to underestimation of water depths near the left bank of the river, toward the end of the study area. However, Case 2 resulted in a narrower channel at the end of the study area, as well as a low velocity zone near the left bank of the river, as presented in Figure 26.

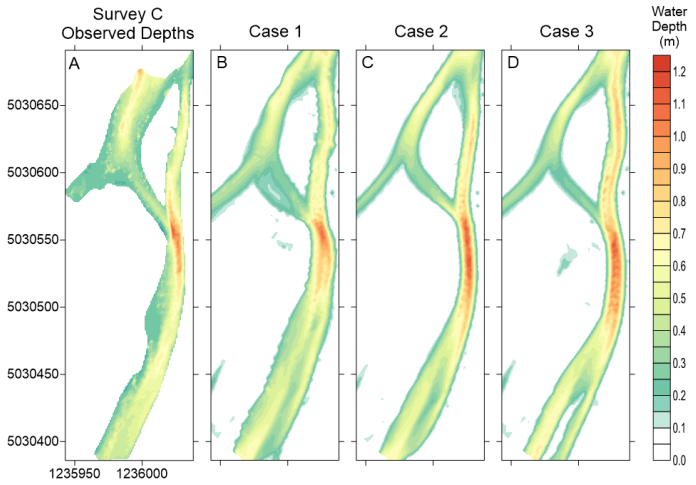

Figure 27 – (A) Observed Depths Distribution Map for Survey C. (B-D) Resulting Depths Distribution Maps of Morphodynamics Simulation for Three Optimal Model Setup Analysis

Lastly, bed elevation distributions from predicted sediment transport using all three cases are shown in Figure 28. All the cases resulted in overprediction of the erosion occurring downstream of the bar, leading to lower bed elevations in that area. Furthermore, the morphology resulting from the use of Case 1 suggests that the predicted channel downstream of the bar was wider than what was observed on the field, as well as lower bed elevation towards the upstream end of the anabranch. On the other hand, Case 1 lead to the best predicted morphology at the end of the study area. Overestimation of sediment deposition toward the left bank did lead to overestimation of the bed levels in that area. However Case 1 model setup did not generate no-flow zones at the very end of the study area contrary to the other cases, as it was previously noted.

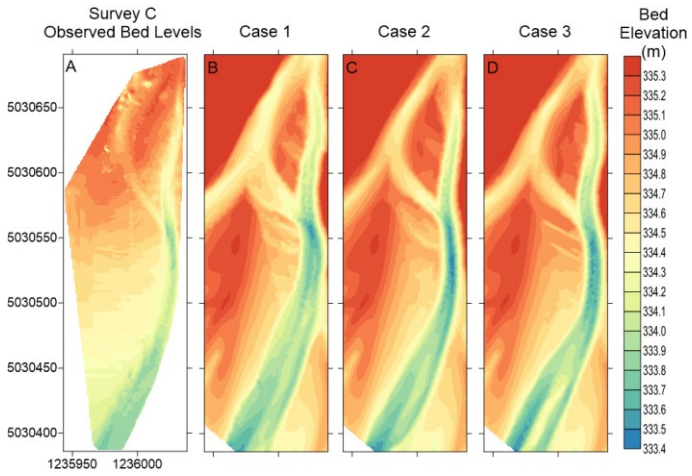

Figure 28 – (A) Observed Bed Levels Distribution Map for Survey C. (B-D) Resulting Bed Levels Distribution Maps of Morphodynamics Simulation for Three Optimal Model Setup Analysis

3.8. Morphodynamic Simulation of Scenario 2

All the analyses that were described previously were done for Scenario 1, thus simulating the morphodynamics that occurred between Surveys B and C. As it was presented, two scenarios were considered in this study. Consequently, Scenario 2 was simulated, using the optimal model setup identified using Scenario 1 (see Section 3.7), to validate the predictive abilities of the Delft3D model. Similarly to Scenario 1, Van Rijn's sediment transport was used to simulate the morphodynamics that were observed in the Rees River anabranch in-between Surveys C and D. Seventy percent (70%) of the total flow entering the anabranch was forced in the upstream boundary B, while the remaining flow was set in the upstream boundary A. Furthermore, an input bedload of 0.0003013 cms was set at the upstream boundary B. The sediment fractions of the forced bedload are medium sand and very fine gravel (Distribution 1).

3.8.1. Numerical Analysis

The following section will present the statistical values obtained when comparing water velocities and depths, estimated from the predicted morphology at the end of Scenario 2, to the observed field data. Moreover, bed elevations predictions will be compared to bed levels observed at Survey D. Table 32 lists the statistical values obtained for the comparison of resulting velocities, depths and bed levels at the end of Scenario 2, as well as the similar values obtained for Scenario 1. Data presented in Table 32 suggest that the model's results for Scenario 1 are somewhat better than for Scenario 2. Indeed, velocity errors were on average approximately 0.12 m/s larger for Scenario 2.

Table 32 – Model's Numerical Performance for Scenario 1 and Scenario 2

	Scenario 1			**Scenario 2**		
Component	**r^2**	**RMSE (unit)**	**MAE (unit)**	**r^2**	**RMSE (unit)**	**MAE (unit)**
Velocity	0.2036	0.4145 (m/s)	0.3418 (m/s)	0.2354	0.5326 (m/s)	0.4653 (m/s)
Depth	0.3983	0.1600 (m)	0.1314 (m)	0.0615	0.1823 (m)	0.1332 (m)
Bed Level	0.8127	0.3111 (m)	0.2717 (m)	0.5733	0.4121 (m)	0.3557 (m)

Similarly, means bed levels errors were approximately 0.08 m larger for Scenario 2 than the errors observed for Scenario 1. One the other hand, water depths estimated from the predicted morphology of Scenario 2 lead to similar errors to the depths estimated for

Scenario 1. To complete the analysis of the model's predictions for Scenario 2, the resulting bedload transports pathways at the end of Scenario 2 were compared to apparent bedload transport pathways derived from Survey D field data. For this analysis, the 63 vector pairs were available for comparison, thus not considered as a large sample size (n > 64). However, since it is very close to the threshold, it was assumed that the significance of the vector correlation coefficient could still be calculated as $\rho_v^2 = 9.488/n$, leading to a value of 0.1506 considered to be significant. As shown in Table 33, the predicted bedload transport pathways obtained for Scenario 2 ($p_v^2 = 0.4800$) were significantly correlated with the apparent bedload transport pathways derived from field data gathered as part of Survey D.

Table 33 – Comparison of Observed Apparent Bedload Transport Pathways to Predicted Bedload Transport Pathways for Both Modelled Scenarios

Scenario	Sample size	Significant p_v^2 value	Calculated p_v^2
Scenario 1	69	0.1375	0.3274
Scenario 2	64	0.1506	0.4800

3.8.2. Visual Interpretation

Distributed maps of the variables discussed and compared in the previous section were computed in order to evaluate the results of Scenario 2 from another angle. First, the velocities estimated from the predicted morphology at the end of the simulation of Scenario 2 were compared to the observed velocity field in Figure 29. The predicted morphology resulted in a generally well predicted velocity field. However, flows in the thalweg region were underestimated, as it was previously shown in Table 32. On the other hand, the flows in the channel on the right side of the bar were in good agreement with the velocities measured during Survey D. The high velocities zone at the confluence of the two channels was

observed towards the right bank of the river, while the predicted morphology leas to higher velocities near the left bank. This misprediction of the high velocities zone contributes to the high mean errors statistics calculated and presented in Table 32. Lastly, the predicted bar width was comparable to the observed bar during Survey D. However, the length of the bar was slightly underestimated by the model.

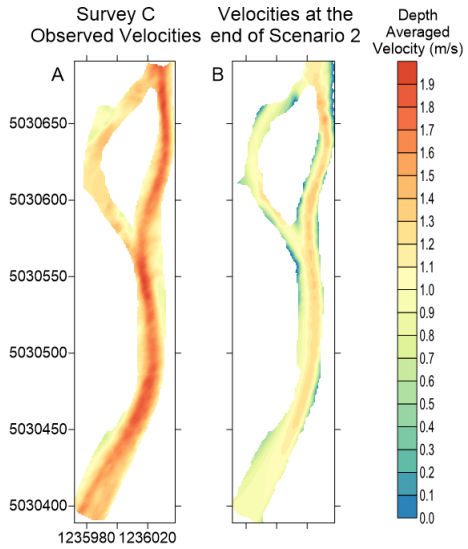

Figure 29 – (A) Observed Velocities Distribution Map for Survey D. (B) Resulting Velocities Distribution Maps of Morphodynamics Simulation of Scenario 2

Similar maps were generated to compare water depths resulting from all three tested cases to the observed depths, as shown in Figure 30. At first glance, the distributed water depths at the end of Scenario 2, estimated from the predicted morphology, show that the deepest section of the river location, downstream of the bar, was mispredicted by the model.

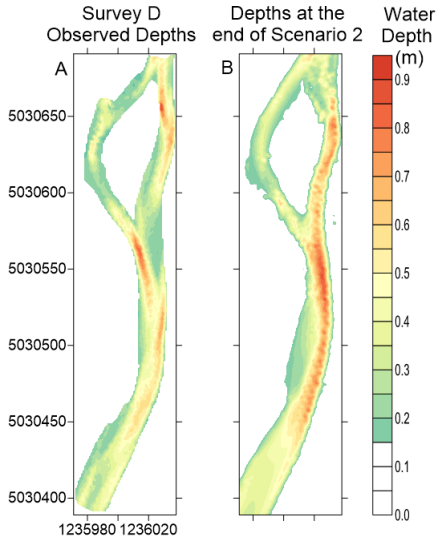

Figure 30 – (A) Observed Depths Distribution Map for Survey D. (B) Resulting Depths Distribution Maps of Morphodynamics Simulation of Scenario 2

Indeed, the deepest section of the river was measured towards the right bank of the river, just downstream of the confluence of the channels. However, the model predicted this zone to be next to the left bank of the river. Furthermore, the predicted morphology resulted in overestimation the water depths downstream of the bar. On the other hand, the general water depth field was in good agreement with the field measurements taken during Survey D. The final bed elevations distribution maps, shown in Figure 31, were generated to visually compare the bed elevations measured during Survey D to the predicted bed levels at the end of Scenario 2. Note that the some errors were generated in the gathering of the topographical data of Survey D, especially in the region on the right side of the bar. Thus, data in that zone was omitted in Figure 31. When comparing the bed levels at the end the morphodynamics simulation of Scenario 2 to the observed bed elevations, it seems that the model's sediment transport predictions overestimated the erosion occurring in the anabranch. Indeed, most of the bed level estimations were lower than observed bed elevations, especially close to the

confluence of the two channels. On the other hand, the predicted morphology was in good agreement with the measured bed levels, only slightly underestimated.

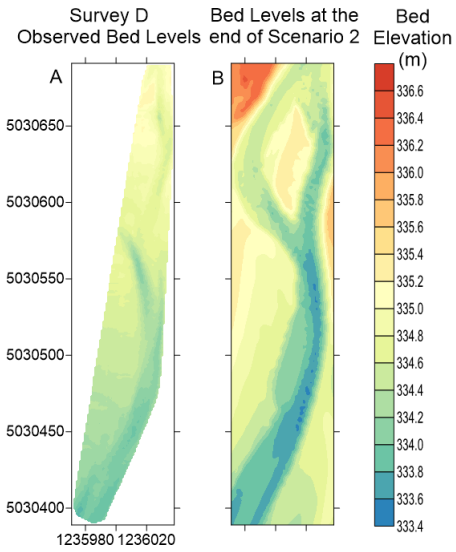

Figure 31 – (A) Observed Bed Levels Distribution Map for Survey D. (B) Resulting Bed Levels Distribution Maps of Morphodynamics Simulation of Scenario 2

4. Discussion

4.1. Optimal Setup for the Delft3D Model

A total of four sediment transport formulas were tested in order to identify the one leading to optimal morphodynamics predictions, as described in Section 3.3. The Van Rijn's sediment transport formula led to the best agreement between the results of the Delft3D model and the observed data gathered on the Rees River. Out of all the results presented in Section 3.3, Figure 13 is the one that leads to the conclusion that the Van Rijn's formula sediment transport predictions were the best out of the tested formulas. Only the Van Rijn's formula replicated the erosion and deposition zones that were observed from Survey B to Survey C. As previously discussed, the use of the Van Rijn's formula mispredicted the channel's

location, however, it did not lead to overestimation of the bed elevations in most parts of the anabranch, in contrast to the predicted morphology resulting from the use of the other tested formulas.

It is interesting that the Van Rijn morphodynamics predictions are the closest to the morphological changes that were noticed in the gravel bed Rees River, as it was developed for sandy rivers. Indeed, the Wilcock-Crowe and Gaueman formulas, designed for transport of gravel-sand mixtures, as well as the Meyer-Peter and Müller formula, developed from gravel transport observations, would have all been good candidates for the modelling of the gravel Rees River. The good morphological predictions by the Van Rijn's for the Rees River can be explained by the fact that it is a simple correlation that links excess shear stress and non-dimensional grain size (Sasal et al. 2008). Thus, even though the Van Rijn formula was derived from work related to sandy rivers, it still can adequately predict morphodynamics at a single anabranch scale in gravel bed rivers. On the other hand, there is still a significant portion of the bed composition which is composed of sand particles, which may advantage the Van Rijn formula. The Van Rijn parameterization was then analyzed to identify the optimal values to use for the Delft3D model. In total, two parameters of the van Rijn formula were tested. The reference level parameter, which can be interpreted as the thickness of the bedload layer, was found to be optimal when using the same 0.04 m value as the bottom roughness. On the other hand, a calibration coefficient, affecting suspended sediment transport, value of 1.00 was found to be optimal for the Rees Delft3D model. Thus, the calibration coefficient does not affect the suspended sediment load calculations.

Initial model runs suggested that the use of two flow boundaries were necessary at the upstream end of the model (see Figure 4). Upstream boundary B is set over the main section of the river where an unsteady discharge per cell is specified, as well as the input sediment

bedload to the model. On the other hand, upstream boundary A is set across the entire width of the river at the upstream end of the model, where the remaining flow (deducted from the discharge set in upstream boundary B) is distributed in the remaining cells. Initially, it was assumed that 60% of the total discharge at the upstream end of the model was forced in upstream boundary B. Further analysis revealed that forcing 70% of the total flow of the river in upstream boundary B leads to better morphodynamic predictions by the model. Sediment transport predictions using discharges fractions lower than 65% mispredicted the bar location or predicted a channel within the bar allowing water to flow through it, which was not observed during the field surveys. However, all tested flow fractions above 55% lead to overestimation of the erosion occurring along the thalweg, due to the high flow forced in this region. Thus, higher flow needed to be forced in the thalweg region of the river in order to replicate the observed morphodynamic between the field surveys. Higher flow leads to higher stream power and erosion potential. Thus, estimated input bedload might be underestimated and larger discharge in the thalweg was required to create substantial sediment transport to replicate the observed morphodynamics. Further calibration might be required to assess whether the input bedload used for both scenarios were sufficient.

Following the sensitivity analysis, three optimal cases were tested to identify the optimal model setup (see Section 3.7). It was found that the best model setup forced 70% of the total flow at the upstream boundary of the model in upstream boundary B, while using medium sand and very fine gravel as the input bedload (Distribution 1). Case 3 used the same 70% of the total flow in upstream boundary B, while using the bedload distribution in which the sediment fractions replicate the ones found in the bed composition (Distribution 2). Simulation of Case 3 lead to excessive deposition at the downstream end of the model, which might be due to the fine sand included in the input bedload. Similarly, more deposition at the

downstream end of the study area was noticed for Case 2 when compared to Case 1, where Case 2 also uses Distribution 2 as the bedload input to the model. Thus, the optimal model setup had more flow in the thalweg region (70% of the total flow), while having less sand (fine sand) in the input bedload.

4.2. Assessment of the Use of Shear Velocity Distribution Maps to Predict Bedload Transport Pathways

Shear velocity, denoted as u_*, is a representation of shear stress using velocity units. It is derived from the theory that velocity distribution can be divided into three flow zones in the turbulence boundary layer. In the zone adjacent to a boundary wall, called the viscous layer, flow is laminar for a very small extent. In this zone, shear stress (τ) is practically constant and can be assumed to be equal to the shear stress at the boundary (τ_0) (Crowe et al., 2009). Thus, in the viscous layer, the change of velocity (u) with respect to flow depth (Y) can be derived as: $\frac{d_u}{d_Y} = \frac{\tau_0}{\mu}$; where μ refers to the dynamic viscosity of the fluid. Integrating the previous equation ($u = \frac{\tau_0 * Y}{\mu}$) and rewriting it using fluid density (ρ), yields: $u = \frac{\sqrt{\tau_0/\rho}}{\nu} Y$, where ν represents kinematic viscosity. The $\sqrt{(\tau_0/\rho)}$ term is the representation of shear velocity, since this term has velocity (m/s) units (Crowe et al., 2009). Keulegan (1938) integrated the log-law of the wall to propose an equation for the shear velocity as a function of water depth, velocity and riverbed grain size. The relationship between shear velocity and the mentioned parameters developed by Keulegan can be represented as: $u_* = \frac{u}{5.75 \log_{10}\left(\frac{12.2Y}{k_S}\right)}$, where D_{90} is the grain size representing 90% of the distribution.

The uncertainty related to the shear velocity is a function of the uncertainty of Y and u, and D_{90}. In the present study, the high precision of the measured bathymetry data led to small water depth uncertainties. It was assumed that it could be neglected when compared to the uncertainty of both u and D_{90}. In order to identify the uncertainty in shear velocity calculations, shear velocity values were calculated based out the uncertainty of water velocity and grain size. First, grain size distribution from 28 sampling sites on the Rees River revealed that the D_{90} of the riverbed is equal to 40.5 ± 21.9 mm (Williams et al., 2013). Thus, shear velocity values were calculated using the maximum and minimal D_{90} of 62.4 mm and 18.6 mm respectively. This discrepancy between possible maximum and minimum D_{90} will translate into the uncertainty of shear velocity. Secondly, shear velocity is also a function of the uncertainty of velocity. The uncertainty of water velocity is related to the uncertainty in each velocity bin measured by the aDcp apparatus. The uncertainty of the depth averaged water velocity was calculated using the method proposed by Rennie and Church (2010), which will be summarized below.

Rennie and Church (2010) based their analysis on an uncertainty model for aDcp velocity measurements. Several error sources were considered by the model. Here, water velocity measurements and turbulent velocity fluctuations were considered for the evaluation of the uncertainty of velocity measurements. Uncertainty of an estimate of mean streamwise velocity out of a single-ping velocity measurement in a single bin, denoted σ_u, was evaluated using velocity measurements error of the aDcp (σ_ϵ) and an estimate of the root-mean-square turbulence intensity for real fluctuations (σ_S). This relation is represented as follows: $\sigma_u^2 = \sigma_\varepsilon^2 + \sigma_S^2$, where σ represents standard deviation. Note that σ_ϵ and σ_S were assumed to be independent. The aDcp velocity error (σ_ϵ) was calculated from the difference between two reductant vertical velocity measurements in a depth bin. Moreover, σ_ϵ accounts for the

Doppler noise and the heterogeneity of the velocities between beams. On the other hand, flow turbulence may increase the heterogeneity of velocity between beams for highly turbulent flows, which might conflict the assumption made by the authors about the independence of σ_ϵ and σ_S. Turbulence intensity (σ_S) was estimated using the empirical equation proposed by Kironoto and Graf (1994). Turbulence intensity is obtained from local shear velocity (u_*) estimates, flow depth (Y) and height above the mean bed elevation (z): $\sigma_s = 2.04\, u_* \exp\left(-0.97\frac{z}{Y}\right)$. Local shear velocity estimates were obtained using the log-law fit to velocity measurements: $u = \frac{u_*}{\kappa}\ln(z) + \frac{u_*}{\kappa}\ln\left(\frac{30}{k_s}\right)$, where κ is the von Karman constant (0.41) and k_s is the bed roughness.

Uncertainty of depth water velocity (σ_U), as was then calculated from single-bin uncertainty as follows: $\sigma_U = \frac{1}{N}\sqrt{C\sum_{i=1}^{N}\sigma_{u_i}^2}$. Parameter N refers to the number of bins in the vertical, while C is the correlation between adjacent bins. Parameter C can be found from the serial correlation theory of Matalas and Langbein (1962): $C = 1 + \frac{2(N-1)}{N}\rho_o$. Adjacent bins employ overlapping measurement volumes, from the Doppler backscatter, and are thus correlated one to the other. Simpson (2001) states that typical correlation, denoted as ρ_o, between two adjacent bins is about 15%, leading to C~1.3. After obtaining an estimation of velocity uncertainty for all survey points, the maximum and minimum velocities can be calculated either by subtracting or adding the calculated uncertainty to the actual velocity measurement.

The maximum shear velocity at a given point is found using the estimated maximum velocity and grain size. Oppositely, to get an estimate of the minimum shear velocity, the minimum velocity and grain size must be used. Keulegan's equation was modified in order

to calculate the maximum and minimum shear velocities for all surveyed points: $u_{*(max,\min)} = \frac{U_{(\max,\min)}}{5.75\log_{10}\left(\frac{12.2Y}{3D_{90}(max,min)}\right)}$. The uncertainty of shear velocity is found by looking at the distribution of the maximum, minimum and estimated shear velocities for all survey points. The estimated shear velocities are calculated using the actual velocity measurement and calculated D_{90} = 40.5 mm. Knowing the maximum and estimated values of shear velocity, the difference between the two values can be computed. Similarly, this can be done using the minimum shear velocities. The mean of the differences calculated were then computed, which represents the standard deviation of the distribution: $diff_{(max,\min)} = u_* - u_{*(max,min)}$.

The shear velocity distributions were calculated using field data of Surveys C and D, thus representing the end conditions of both scenarios. However, instead of using the D_{90} value found from the sediment samplings, the roughness term ($3D_{90}$) shown in Keulegan's equation was estimated. As discussed in Section 3.1, Williams et al. (2013) found that a roughness length of 0.04 m was optimal for the modelling of the braided Rees River. This value was used to calculate shear velocity distributions for both Surveys C and D and these were plotted as shown by Figure 32 – (A-B) Shear Velocity Distribution Maps Showing Calculated Uncertainty Bands. The mean shear velocities of those distributions are 0.1026 m/s and 0.1098 m/s, respectively for Surveys C and D. From those values and the calculated standard deviations, shear velocity uncertainties were calculated.

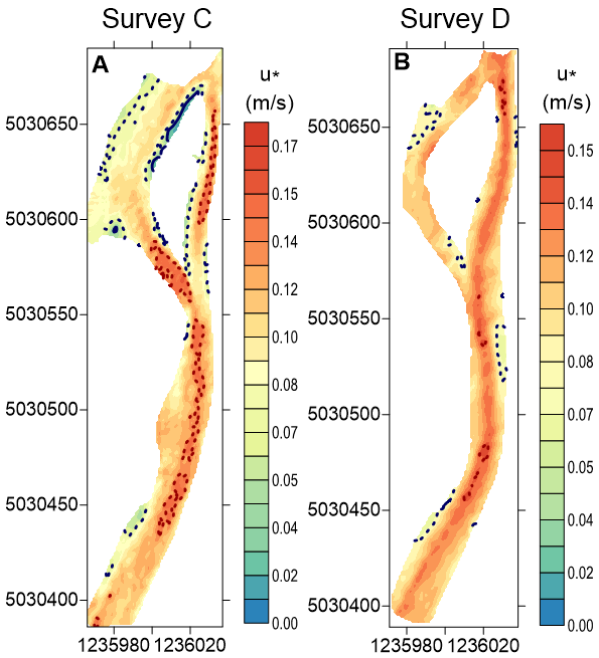

Figure 32 – (A-B) Shear Velocity Distribution Maps Showing Calculated Uncertainty Bands. Highlighted areas are either high shear stress (Red) or low shear stress (Blue) zones

Uncertainty bands calculated are included in the distribution maps. Areas enclosed by dotted lines represent shear velocities either one-standard deviation above or below the mean of the distribution. Similarly, areas circled by solid lines are shear velocities that are two-standard deviations away from the distribution's mean. Thus, highlighted areas are the zones which can be described as either high shear stress or low shear stress zones with confidence. The shear velocity maps that are presented in Figure 32 were converted to shear stress distribution maps and compared to the predicted bed shear stress distribution maps at the end of both scenarios to assess the predictive abilities of the Delft3D model regarding shear stress predictions. Figure 33 shows the comparison of the observed and predicted shear distributions for both scenarios. In most cases, the areas of high shear stress predicted by the model correspond to the areas of high observed shear.

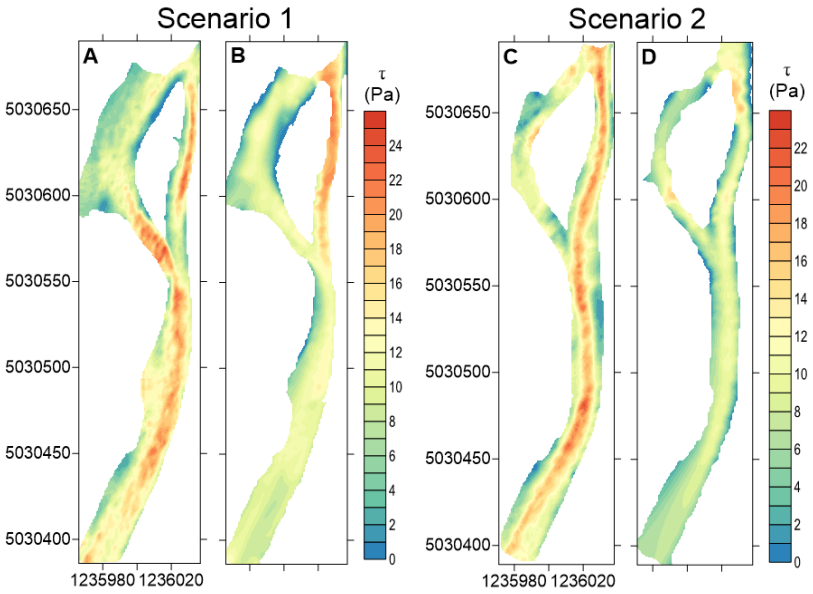

Figure 33 – (A) Observed Shear Stress Distribution Map for Survey C (B) Predicted Shear Stress Distribution Map at the End of Scenario 1 (C) Observed Shear Stress Distribution Map for Survey D (D) Predicted Shear Stress Distribution Map at the End of Scenario 2

Indeed, the high shear stresses observed near the upstream end of the main channel during Survey C (Figure 33 A) are well predicted by the model, as shown in Figure 33 B. However, the high shear stress zone that was observed near the confluence of the two channels during Survey C (Figure 33 A) was not captured by the model. On the other hand, the shear stress distribution during Survey D shown in Figure 33 C was generally well predicted by the Delft3D model. However, downstream of the bar, the predicted high shear stress zones was towards the left bank of the river, while field measurements suggest that the high shear stress zones were located towards the right bank. Thus, model results related to shear stress predictions were generally in good agreement with the field data, but not always. As previously discussed, conventional 2D morphodynamics models will predict bedload

transport from the shear stress distribution. However, sediment supply locations can dictate bedload transport pathways in some occasions. Thus, predicted bedload transport pathways by the model were compared to the apparent bedload velocity observed during both Surveys C and D through vector correlation analysis (see Section 2.5). It was found that the bedload pathways predicted by the model were significantly correlated with the apparent bedload velocity pathways derived from field measurements (see Section 3.8.1). Figure 34 visually compares the observed and predicted bedload pathways. As shown, the predicted bedload pathways were generally not resolved correctly and not in good agreement with the observed apparent bedload velocity.

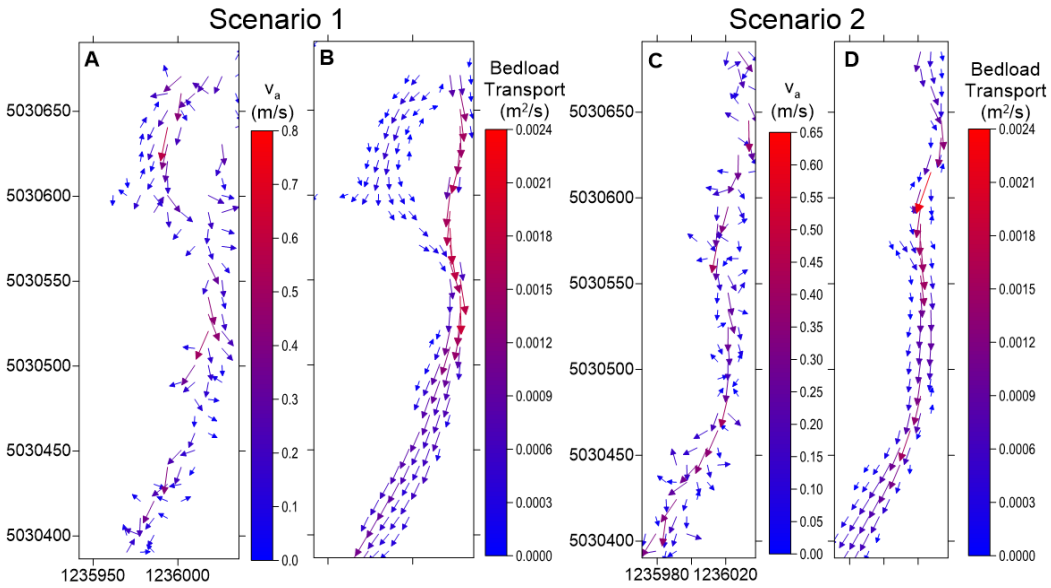

Figure 34 – (A) Apparent Bedload Velocity Vectors Observed as part of Survey C (B) Predicted Bedload Transport Pathways Vectors at the End of Scenario 1 (C) Apparent Bedload Velocity Vectors Observed as part of Survey D (D) Predicted Bedload Transport Pathways Vectors at the End of Scenario 2

On one hand, model predictions, for Scenario 1, of high bedload transport were towards the left side of the bar, while they were observed on the right side of the bar during the field surveys. On the other, the main bedload pathways downstream of the bar were well predicted (Figure 34 B). Similar conclusions can be drawn comparing the apparent bedload velocity vectors for Survey D (Figure 34 C) to the model predictions of Scenario 2 (Figure 34 D). The bedload predictions were correct on the left side of the bar, but did not transition to the other side of the channel near the downstream end of the study area.

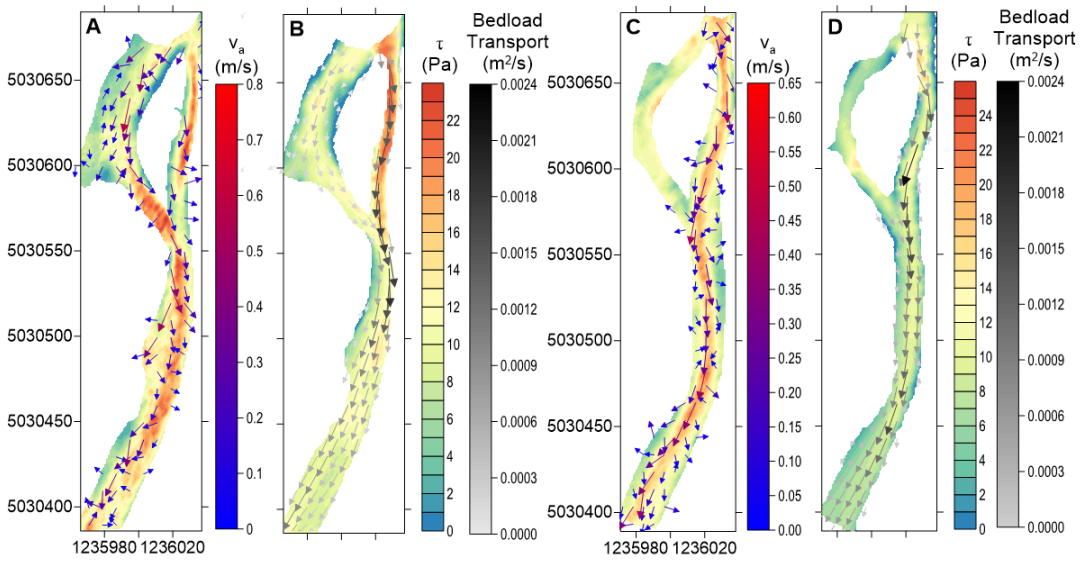

Figure 35 – (A) Observed Shear Stress Distribution Map of Survey C Overlaid by Observed Bedload Transport Pathways (B) Predicted Shear Stress Distribution Map Overlaid by Predicted Bedload Transport Pathways from Morphodynamic Simulation of Scenario 1 (C) Observed Shear Stress Distribution Map of Survey D Overlaid by Observed Bedload Transport Pathways (D) Predicted Shear Stress Distribution Map Overlaid by Predicted Bedload Transport Pathways from Morphodynamic Simulation of Scenario 2. Note that the first shear stress scale is valid for sub plots A and B, while the second shear stress scale is for sub plots C and D.

Finally, predicted bedload transport pathways and shear stress distribution maps at the end of both scenarios were plotted along with the observed shear stress distribution maps presented in Figure 33. This was done in an attempt to assess whether high bedload transport is correlated with high shear stress. Figure 35 suggests that, in most cases, areas of high shear stress were the zones where highest bedload transport was predicted by the model (Figure 35 B and D). Furthermore, predictions of high shear stress zones by the model generally agreed with the observed locations of high shear. However, in areas where high shear stress was not well predicted by the model, bedload transport was not substantial, such as the zone just before the confluence of the two channels for Survey C (Figure 35 A). Figure 35 shows that the predicted bedload transport pathways locations were highly dependent of the high predicted shear stress areas. Furthermore, observed bedload transport pathways were not always correlated to the observed apparent bedload velocity presented in Figure 34. Thus, the sediment transport that was observed may not be due to high shear stress and this implies that some other sediment supply sources are in action.

5. Summary and Conclusion

The present study discussed about the calibration of a Delft3D model used to simulate morphological changes occurring in a 300 m anabranch of New Zealand's Rees River. First, simulations were done to validate the hydraulic parameters, which were found as part of Williams et al. (2013). These model runs were done considering only flow simulation, thus not including morphodynamic simulations. A bottom roughness value of 0.04 m was found to be optimal for the Delft3D model, which is in agreement with the value found by Williams

et al. (2013). Furthermore, the optimal eddy viscosity for this Delft3D model of the Rees River is 0.100 m^2/s, again in agreement with the findings by Williams et al. (2013).

The model was then calibrated for morphodynamic simulations. The first step was to identify the sediment transport formula which would lead to the best model predictions. Out of the four sediment transport formulas that were investigated, the Meyer-Peter and Müller formula led to smaller mean errors for all analyzed variables, namely water velocity, water depth and bed elevation. Thus, a point-to-point comparison between observed and modelled data leads to better statistics using the Meyer-Peter and Müller formula. However, when comparing modelled results and observed data using distribution maps, the velocities, depths and bed levels are best reproduced by the Van Rijn formula. In other words, morphodynamic predictions using the Van Rijn sediment transport formula generally yielded correct widths and depths of anabranch channels, but the channels were spatially offset from their observed locations. The spatial offset resulted in low statistical comparison of the Van Rijn results on a point-to-point basis to observed data. Overall, the Van Rijn's formula was found to be the one leading to best agreement between observed data and model predictions, despite occasionally leading to lower statistical values.

Further sensitivity analyses were done using the Van Rijn's formula to calibrate the Delft3D model. First, sensitivity analysis and calibration were done on the Van Rijn formula parameters of reference level and calibration coefficient. It was found that the initial assumptions for the mentioned parameters, namely a reference level equal to the bottom roughness value (0.040 m) used by the model (see Section 3.1), and a calibration coefficient of 1.00, lead to the best morphodynamic predictions in the study area. Secondly, several analyses were done to look at the impact of different settings used at the upstream boundary of the model. Two flow boundaries were used at the upstream end of the model. One

boundary (upstream boundary A) covered the entire width of the river, while the second boundary (upstream boundary B) was limited to the main section of the river (thalweg). Discharge at the upstream boundary of the model was estimated from the flow measurements performed at the Invincible gauging station, located 8 km upstream of the study area (see Section 2.4). A discharge per cell was forced in upstream boundary B, while total discharge was forced in upstream boundary A. Sensitivity analysis was done to identify what percentage of flow to be forced in the main region of the river, thus in upstream boundary B, would lead to better morphodynamic predictions. It was found that forcing 70% of the total flow at the upstream boundary B generated the best model predictions. This means that the sum of the discharge per cell forced in the upstream boundary B's cells at each timestep is equal to 70% of the estimated flow, while the remaining 30% of the discharge is distributed in the remaining cells of upstream boundary A (i.e. the cells not overlaid by upstream boundary B). Another sensitivity analysis related to the upstream boundary is linked to the sediment distribution of the input bedload forced to the model (see Section 2.4). It was found that the sediment distribution leading to the optimal model predictions is the one for which the sediment fractions are in the same proportion as the bed composition.

However, when comparing the best model runs one to the other, it was found that the optimal setting of the Delft3D model forces 70% of the total estimated flow in upstream boundary B, while using the initial guess of the sediment distribution of the bedload input to the model, which consists of half medium sand and half very fine gravel.

Using the model setting described above, predicted bedload transport pathways were found to be significantly correlated with the apparent bedload transport pathways derived from the field measurements of Surveys C and D. Indeed, the morphodynamic simulations of both tested scenarios lead to bedload vectors correlation coefficients of 0.3274 and 0.4800,

respectively for Scenario 1 and 2, greater than the threshold value for significance of 0.1375 and 0.1506 for Scenario 1 and 2, respectively. However, the model was incapable of reproducing all observed bedload pathways in the model domain, which can be attributed to the influence of sediment supply sources on the observed pathways.

The calibrated model was ultimately used to assess whether shear stress distributions are useful to predict bedload transport pathways. Predicted bedload transport pathways, at the end of both scenarios, were plotted against shear velocity distribution maps derived from field measurement data. This analysis was done to assess the correlation between the predicted bedload pathways locations of the Delft3D model and the high shear stress zones derived from field observations. It was found that, in most cases, highest bedload transport is predicted by the model in the areas of high observed shear stress zones. Thus, there is a good correlation between high observed shear stress and high predicted bedload transports. However, the predicted bedload transport pathways are highly dependent of the adequate prediction of high shear stress zones. On the other hand, some of the high bedload transport pathways observed as part of the field surveys (Figure 34) are not located in high shear areas, thus linked to other sources of sediment supply.

6. References

Ashmore, P., (2013). Morphology and dynamics of braided rivers In Treatise on Geomorphology, edited by John F. Shroder, Academic Press, San Diego, Vol. 9, 289–312 ISBN 9780080885223

Belletti, B., Dufour, S., and Piégay, H. (2015). What is the Relative Effect of Space and Time to Explain the Braided River Width and Island Patterns at a Regional Scale?. River Research and Applications, 31(1), 1-15.

Bertoldi, W., Zanoni, L., & Tubino, M. (2010). Assessment of morphological changes induced by flow and flood pulses in a gravel bed braided river: the Tagliamento River (Italy). Geomorphology, 114(3), 348-360.

Brasington, J., Rennie, C.D., Vericat, D., Williams, R., Goodsell, B., Hicks, M., Batalla, R. (2011) Monitoring Braided River Morphodynamics with an Acoustic Doppler Current Profiler, 34th IAHR 2011 Congress, Brisbane.

Cao, Z. and Carling, P.A. (2003). Mathematical modelling of alluvial rivers: reality and myth. Part 1: General review. Proc. Inst. Civil Engineers, Water and Maritime Eng. 154(3):207-219.

Caruso, B. S., Edmondson, L., & Pithie, C. (2013). Braided river flow and invasive vegetation dynamics in the Southern Alps, New Zealand Environmental management, 52(1), 1-18.

Chalov, S. R., and Alexeevsky, N. I. (2015). Braided rivers: structure, types and hydrological effects. Hydrology Research, 46(2), 258-275.

Chang, H. H. (1994). Test and calibration of FLUVIAL-12 model using data from the San Dieguito River. Rep Prepared for Southern California Edison Company.

Chang, H. H., Harrison, L. L., Lee, W., & Tu, S. (1996). Numerical modelling for sediment-pass-through reservoirs. Journal of Hydraulic Engineering, 122(7), 381-388.

Chen, D., & Duan, J. G. (2008). Case study: Two-dimensional model simulation of channel migration processes in West Jordan River, Utah. Journal of Hydraulic Engineering, 134(3), 315-327.

Church, M., D. G. McLean, and J. F. Walcott (1987). River bed gravels: sampling and analysis. Sediment Transport in Gravel-Bed Rivers, 43-88

Church, M. (1992) Channel morphology and typology. In: Calow, P. and Petts, G.E. (eds.) The Rivers Handbook. Blackwell, Oxford, pp. 126–143

Cook, S. J., D. J. Quincey, and J. Brasington (2013), Geomorphology of the Rees Valley, Otago, New Zealand, J. Maps

Crosby D.S., Breaker L.C., Gemmill W.H. (1993). A proposed definition for vector correlation in geophysics: theory and application. Journal of Atmospheric and Oceanic Technology 10: 355–367.

Crowe, C. T., Elger, D. F., Williams, B. C., Roberson, J. A. (2009), Engineering Fluid Mechanics, John Wiley & Sons, Inc., 9th edition, 293.

Danish Hydraulic Institute (DHI). (1999). MIKE21C user's guide and scientific documentation. Rep., DHI, Horsholm, Denmark.

Deltares (2014). Delft3D-FLOW, Simulation of multi-dimensional hydrodynamic flows and transport phenomena, including sediments, User Manual. Version 3.15.34158

Fang, C.-M. (2003). Simulation of Bend Secondary Flow Effect in 2D Depth-averaged Model, Journal of China Institute of Water Resources and Hydropower Research, Vol. 1, No.3.

Gaeuman, D., Andrews, E. D., Krause, A., & Smith, W. (2009). Predicting fractional bed load transport rates: Application of the Wilcock-Crowe equations to a regulated gravel bed river. Water resources research, 45(6).

Gomez, B., and Church, M. (1989). An assessment of bed load sediment transport formulae for gravel bed rivers. Water Resources. Res., 25(6), 1161-1186.

Islam, A. S. (2009). Gravel transport and morphological modeling for the Lower Fraser River, British Columbia (Doctoral dissertation, University of British Columbia (Vancouver).

Keulegan, G. H. (1938). Laws of turbulent flow in open channels (Vol. 21, pp. 707-741). US: National Bureau of Standards.

Kironoto, B. A., and W. Graf (1994), Turbulence characteristics in rough uniform open-channel flow, Proc. Inst. Civ. Eng., 106, 333–344, doi:10.1680/iwtme.1994.27234

Klingeman, P. C., and W. W. Emmett (1982). Gravel bedload transport processes, in Gravel Bed Rivers. Edited by R. D. Hey, J. C. Bathurst and C. R. Thorne. Wiley, London. 141-179

Klingeman, P. C., C. J. Chaquette, and S. B. Hammond (1979). Bed material characteristics near Oak Creek Sediment Transport Research Facilities, 1978-1979. Oak Creek Sediment Transport Report BM3. Water Resources Research Institute. Oregon State University. Oregon.

Lane, S. N., Bradbrook, K. F., Richards, K. S., Biron, P. A., & Roy, A. G. (1999). The application of computational fluid dynamics to natural river channels: three-dimensional versus two-dimensional approaches.Geomorphology, 29(1), 1-20.

Lee, H. Y., Hsieh, H. M., Yang, J. C., & Yang, C. T. (1997). Quasi-two-dimensional simulation of scour and deposition in alluvial channels. Journal of Hydraulic Engineering, 123(7), 600-609.

Li, S. S., & Millar, R. G. (2007). Simulating bed-load transport in a complex gravel-bed river. Journal of Hydraulic Engineering.

Li, S. S., Millar, R. G., & Islam, S. (2008). Modelling gravel transport and morphology for the Fraser river gravel reach, British Columbia. Geomorphology, 95(3), 206-222.

Matalas, N. C., and W. B. Langbein (1962), Information content of the mean, J. Geophys. Res., 67(9), 3441–3448, doi:10.1029/JZ067i009p03441.

Meyer-Peter, E. and R. Müller (1948). Formulas for bed load transport. In Proceedings of the 2nd Congress IAHR, Stockholm, vol. 2, 39–64

Murray, A.B., Paola, C., (1994). A cellular model of braided rivers. Nature 371, 54–57.

Nicholas, A. P. (2003). Investigation of spatially distributed braided river flows using a two-dimensional hydraulic model. Earth Surface Processes and Landforms, 28(6), 655-674.

Nicholas, A. (2013). Morphodynamic Modeling of Rivers and Floodplains, In Treatise on Geomorphology, edited by John F. Shroder, Academic Press, San Diego, , Vol. 9, 160-179, ISBN 9780080885223

Papanicolaou, A. N., Elhakeem, M., Krallis, G., Prakash, S., & Edinger, J. (2008). Sediment transport modeling review—current and future developments. Journal of Hydraulic Engineering, 134(1), 1-14.

Rennie C. D. (2002). Non-invasive measurement of fluvial bedload transport velocity using an acoustic Doppler current profiler. PhD thesis, Department of Civil Engineering, University of British Columbia, Canada.

Rennie, C.D. (2012). Mapping water and sediment flux distributions in gravel-bed rivers using aDcps. in Gravel-bed rivers: processes, tools, environments. Church, M., Biron, P. and Roy, A.G., editors. Chichester, John Wiley & Sons. ISBN 978-0-470-68890-8.

Rennie, C. D., and M. Church (2010), Mapping spatial distributions and uncertainty of water and sediment flux in a large gravel bed river reach using an acoustic Doppler current profiler, J. Geophys. Res., 115, F03035, doi:10.1029/2009JF001556.

Rennie, C.D., Millar, R.G., Church, M.A., (2002) Measurement of bedload velocity using an acoustic Doppler current profiler. Journal of Hydraulic Engineering (ASCE). 128:473-483.

Rennie, C. D., and R. G. Millar (2004). Measurement of the spatial distribution of fluvial bedload transport velocity in both sand and gravel, Earth Surf. Processes Landforms, 29(10), 1173–1193

Sasal, M., Kashyap, S., Rennie, C.D., Nistor, I. Artificial Neural Network for bedload estimation in alluvial rivers, Journal of Hydraulic Research, 47(2):223–232, 2009.

Simpson, M. R. (2001), Discharge measurements using a broad-band acoustic Doppler current profiler, U.S. Geol. Surv. Open File Rep. 01-1.

Spasojevic, M., & Holly Jr, F. M. (1990). 2-D bed evolution in natural watercourses-New simulation approach. Journal of Waterway, Port, Coastal, and Ocean Engineering, 116(4), 425-443.

Struiksma, N. (1985). Prediction of 2-D bed topography in rivers. Journal of Hydraulic Engineering, 111(8), 1169-1182.

Van Rijn, L. C. (1984a). Sediment transport, part I: bed load transport. Journal of hydraulic engineering, 110(10), 1431-1456.

Van Rijn, L. C. (1984b). Sediment transport, part II: suspended load transport.Journal of hydraulic engineering, 110(11), 1613-1641.

Van Rijn, L. C. (1984c). Sediment transport, part III: bed forms and alluvial roughness. Journal of hydraulic engineering, 110(12), 1733-1754.

Van Rijn, L. C. (1993). Principles of sediment transport in rivers, estuaries and coastal seas (Vol. 1006). Amsterdam: Aqua publications.

Vasquez, J. A. (2005). Two-dimensional finite element river morphology model., Ph.D. thesis, Univ. of British Columbia, Vancouver, B.C. Canada.

Vasquez, J. A., Millar, R. G., and Steffler, P. M. (2005). River2D morphology. Part I: Straight alluvial channels. Proc., 17th Canadian Hydrotechnical Conf., CSCE, Edmonton, Alta., Canada, 249–258.

Vasquez, J. A., & Leal, J. G. (2006). Two-dimensional dambreak simulation over movable beds with an unstructured mesh. Ferreira, Alves, Leal & Cardoso (ed.) River Flow, 2, 1483-1491.

Vasquez, J. A., Millar, R. G., & Steffler, P. M. (2007). Two-dimensional finite element river morphology model. Canadian Journal of Civil Engineering, 34(6), 752-760.

Vasquez, J. A., Steffler, P. M., & Millar, R. G. (2008). Modeling bed changes in meandering rivers using triangular finite elements. Journal of Hydraulic Engineering, 134(9), 1348-1352.

Wang, G., Xia, J., & Wu, B. (2008). Numerical simulation of longitudinal and lateral channel deformations in the braided reach of the lower Yellow River.Journal of Hydraulic Engineering, 134(8), 1064-1078.

Walstra, D. J., van Rijn, L. C., and Aarninkhof, S. G. (1998). Sand transport at the lower shoreface of the Dutch coast. Technical Rep. Z, 2378.

Walters, W. H., Ecker, R. M., and Onishi, Y. (1982). Sediment and Radionuclide Transport in Rivers: Phase 2 field sampling program for Cattaraugus and Buttermilk Creeks, New York. Technical Rep. No. PNL-3117, Vol. 2, Pacific Northwest Lab., Richland, Wash.

Wilcock, P. R., and Crowe, J. C. (2003). Surface-based transport model for mixed-size sediment. Journal of Hydraulic Engineering, 129(2), 120-128.

Williams, R. D., (2014). Two-dimensional Numerical Modelling of Natural Braided River Morphodynamics. PhD Thesis, Aberystwyth University, Aberystwyth, Ceredigion, UK

Williams, R. D., Brasington, J., Hicks, M., Measures, R., Rennie, C. D., & Vericat, D. (2013). Hydraulic validation of two-dimensional simulations of braided river flow with spatially continuous aDcp data. Water Resources Research, 49(9), 5183-5205.

Williams, R. D., C. D. Rennie, J. Brasington,D. M. Hicks, and D. Vericat (2015), Linking the spatial distribution of bed load transport to morphological change during high-flow events in a shallow braided river, J. Geophys. Res. Earth Surf.,120, 604–622

Wolman, M. G. (1954), A method of sampling coarse bed material, Trans. AGU, 35, 951–956.

Zar, J. H. (1996), Biostatistical Analysis, 3rd edition, Prentice Hall, Upper Saddle River, NJ.

2. Conclusion and Recommendations

The presented journal paper discussed the work that was accomplished during this research project. A morphodynamic model, namely Delft3D, was used to simulate morphological changes that were observed in an anabranch of the braided Rees River located in New Zealand. Field data obtained from three field surveys were used as initial conditions and for comparison purposes to assess the model's performance. Water velocities, depths and bed levels at the end of the morphodynamic simulations were compared to observed field data to evaluate the optimal model setup for the modelling of the Rees River anabranch.

Ultimately, the model was used to investigate whether shear stress distributions are useful tools to predict bedload transport pathways. Apparent bedload velocity derived from field data were compared to predicted model transport pathways. It was found that the model's predictions related to sediment transport pathways were significantly correlated to the observed field pathways. Furthermore, predicted bedload transport pathways, at the end of morphodynamic simulation, were plotted against shear velocity distribution maps derived from field measurement data. It was found that, generally, high bedload transport is predicted in the areas of high observed shear stress zones. However, the predicted bedload transport pathways were highly dependent of the high shear stress zones. Thus, adequate prediction of shear stress distribution in the anabranch is essential in order to obtain good agreement between observed bedload transport pathways and modelled predictions. On the other hand, it was found that high observed sediment transport is not always linked to high shear stress. Thus, results from this work imply that the use of a robust bank erosion algorithm is essential to adequately predict observed bedload transport pathways. The model's predictions of bedload transport were in good agreement with observed field data where the model's

predictions of high shear stress were comparable to field observations. However, predictions of substantial bedload transport in areas of low shear stress were not captured by the model, which suggest that the observed pathways were not due to high shear, but rather to other sediment supply sources.

Further work linked to this project would include the calibration of the magnitude of the input bedload. Moreover, the use of a new bank erosion algorithm that accounts for sediment transport related to the repose angle of the sediment related to the angle of the banks should be investigated. This was initially pointed out by Williams (2014) and currently being implemented by Richard Measures, hydrodynamics scientist at the National Institute of Water and Atmospheric Research in New Zealand.

3. References

Ashmore, P., (2013). Morphology and dynamics of braided rivers In Treatise on Geomorphology, edited by John F. Shroder, Academic Press, San Diego, Vol. 9, 289–312 ISBN 9780080885223

Belletti, B., Dufour, S., and Piégay, H. (2015). What is the Relative Effect of Space and Time to Explain the Braided River Width and Island Patterns at a Regional Scale?. River Research and Applications, 31(1), 1-15.

Bertoldi, W., Zanoni, L., & Tubino, M. (2010). Assessment of morphological changes induced by flow and flood pulses in a gravel bed braided river: the Tagliamento River (Italy). Geomorphology, 114(3), 348-360.

Cao, Z. and Carling, P.A. (2003). Mathematical modelling of alluvial rivers: reality and myth. Part 1: General review. Proc. Inst. Civil Engineers, Water and Maritime Eng. 154(3):207-219.

Caruso, B. S., Edmondson, L., & Pithie, C. (2013). Braided river flow and invasive vegetation dynamics in the Southern Alps, New Zealand Environmental management, 52(1), 1-18.

Chalov, S. R., and Alexeevsky, N. I. (2015). Braided rivers: structure, types and hydrological effects. Hydrology Research, 46(2), 258-275.

Chang, H. H. (1994). Test and calibration of FLUVIAL-12 model using data from the San Dieguito River. Rep Prepared for Southern California Edison Company.

Chang, H. H., Harrison, L. L., Lee, W., & Tu, S. (1996). Numerical modelling for sediment-pass-through reservoirs. Journal of Hydraulic Engineering, 122(7), 381-388.

Chen, D., and Duan, J. G. (2008). Case study: Two-dimensional model simulation of channel migration processes in West Jordan River, Utah. Journal of Hydraulic Engineering, 134(3), 315-327.

Church, M. (1992) Channel morphology and typology. In: Calow, P. and Petts, G.E. (eds.) The Rivers Handbook. Blackwell, Oxford, pp. 126–143

Deltares (2014). Delft3D-FLOW, Simulation of multi-dimensional hydrodynamic flows and transport phenomena, including sediments, User Manual. Version 3.15.34158

Fang, C.-M. (2003). Simulation of Bend Secondary Flow Effect in 2D Depth-averaged Model, Journal of China Institute of Water Resources and Hydropower Research, Vol. 1, No.3.

Gomez, B., and Church, M. (1989). An assessment of bed load sediment transport formulae for gravel bed rivers. Water Resources. Res., 25(6), 1161-1186.

Islam, A. S. (2009). Gravel transport and morphological modeling for the Lower Fraser River, British Columbia (Doctoral dissertation, University of British Columbia (Vancouver).

Lane, S. N., Bradbrook, K. F., Richards, K. S., Biron, P. A., & Roy, A. G. (1999). The application of computational fluid dynamics to natural river channels: three-dimensional versus two-dimensional approaches.Geomorphology, 29(1), 1-20.

Lee, H. Y., Hsieh, H. M., Yang, J. C., & Yang, C. T. (1997). Quasi-two-dimensional simulation of scour and deposition in alluvial channels. Journal of Hydraulic Engineering, 123(7), 600-609.

Li, S. S., & Millar, R. G. (2007). Simulating bed-load transport in a complex gravel-bed river. Journal of Hydraulic Engineering.

Li, S. S., Millar, R. G., & Islam, S. (2008). Modelling gravel transport and morphology for the Fraser river gravel reach, British Columbia. Geomorphology, 95(3), 206-222.

Murray, A.B., Paola, C., (1994). A cellular model of braided rivers. Nature 371, 54–57

Nicholas, A. P. (2003). Investigation of spatially distributed braided river flows using a two-dimensional hydraulic model. Earth Surface Processes and Landforms, 28(6), 655-674.

Nicholas, A. (2013). Morphodynamic Modeling of Rivers and Floodplains, In Treatise on Geomorphology, edited by John F. Shroder, Academic Press, San Diego, , Vol. 9, 160-179, ISBN 9780080885223

Papanicolaou, A. N., Elhakeem, M., Krallis, G., Prakash, S., & Edinger, J. (2008). Sediment transport modeling review—current and future developments. Journal of Hydraulic Engineering, 134(1), 1-14.

Rennie C. D. (2002). Non-invasive measurement of fluvial bedload transport velocity using an acoustic Doppler current profiler. PhD thesis, Department of Civil Engineering, University of British Columbia, Canada.

Rennie, C.D. (2012). Mapping water and sediment flux distributions in gravel-bed rivers using aDcps. in Gravel-bed rivers: processes, tools, environments. Church, M., Biron, P. and Roy, A.G., editors. Chichester, John Wiley & Sons. ISBN 978-0-470-68890-8.

Rennie, C. D., and M. Church (2010), Mapping spatial distributions and uncertainty of water and sediment flux in a large gravel bed river reach using an acoustic Doppler current profiler, J. Geophys. Res., 115, F03035, doi:10.1029/2009JF001556.

Rennie, C.D., Millar, R.G., Church, M.A., (2002) Measurement of bedload velocity using an acoustic Doppler current profiler. Journal of Hydraulic Engineering (ASCE). 128:473-483.

Rennie, C. D., and R. G. Millar (2004). Measurement of the spatial distribution of fluvial bedload transport velocity in both sand and gravel, Earth Surf. Processes Landforms, 29(10), 1173–1193

Spasojevic, M., & Holly Jr, F. M. (1990). 2-D bed evolution in natural watercourses-New simulation approach. Journal of Waterway, Port, Coastal, and Ocean Engineering, 116(4), 425-443.

Struiksma, N. (1985). Prediction of 2-D bed topography in rivers. Journal of Hydraulic Engineering, 111(8), 1169-1182

Van Rijn, L. C. (1984a). Sediment transport, part I: bed load transport. Journal of hydraulic engineering, 110(10), 1431-1456.

Van Rijn, L. C. (1984b). Sediment transport, part II: suspended load transport.Journal of hydraulic engineering, 110(11), 1613-1641.

Van Rijn, L. C. (1984c). Sediment transport, part III: bed forms and alluvial roughness. Journal of hydraulic engineering, 110(12), 1733-1754.

Vasquez, J. A. (2005). Two-dimensional finite element river morphology model., Ph.D. thesis, Univ. of British Columbia, Vancouver, B.C. Canada.

Vasquez, J. A., Millar, R. G., and Steffler, P. M. (2005). River2D morphology. Part I: Straight alluvial channels. Proc., 17th Canadian Hydrotechnical Conf., CSCE, Edmonton, Alta., Canada, 249–258.

Vasquez, J. A., & Leal, J. G. (2006). Two-dimensional dambreak simulation over movable beds with an unstructured mesh. Ferreira, Alves, Leal & Cardoso (ed.) River Flow, 2, 1483-1491.

Vasquez, J. A., Millar, R. G., & Steffler, P. M. (2007). Two-dimensional finite element river morphology model. Canadian Journal of Civil Engineering, 34(6), 752-760.

Vasquez, J. A., Steffler, P. M., & Millar, R. G. (2008). Modeling bed changes in meandering rivers using triangular finite elements. Journal of Hydraulic Engineering, 134(9), 1348-1352.

Walstra, D. J., van Rijn, L. C., and Aarninkhof, S. G. (1998). Sand transport at the lower shoreface of the Dutch coast. Technical Rep. Z, 2378.

Walters, W. H., Ecker, R. M., and Onishi, Y. (1982). Sediment and Radionuclide Transport in Rivers: Phase 2 field sampling program for Cattaraugus and Buttermilk Creeks, New York. Williams, R. D., (2014). Two-dimensional Numerical Modelling of Natural Braided River Morphodynamics. PhD Thesis, Aberystwyth University, Aberystwyth, Ceredigion, UK

Wang, G., Xia, J., & Wu, B. (2008). Numerical simulation of longitudinal and lateral channel deformations in the braided reach of the lower Yellow River.Journal of Hydraulic Engineering, 134(8), 1064-1078.

Williams, R. D., C. D. Rennie, J. Brasington,D. M. Hicks, and D. Vericat (2015), Linking the spatial distribution of bed load transport to morphological change during high-flow events in a shallow braided river, J. Geophys. Res. Earth Surf.,120, 604–622